

DISENTANGLING THE AGN AND STAR-FORMATION CONTRIBUTIONS TO THE RADIO-X-RAY
EMISSION OF RADIO-LOUD QUASARS AT $1 < Z < 2$ MOJEGAN AZADI¹, BELINDA WILKES¹, JOANNA KURASZKIEWICZ¹, JONATHAN McDOWELL¹, RALF SIEBENMORGEN²,
MATTHEW ASHBY¹, MARK BIRKINSHAW³, DIANA WORRALL³, NATASHA ABRAMS¹, PETER BARTHEL⁴, GIOVANNI FAZIO¹,
MARTIN HAAS⁵, SÓLEY HYMAN⁶, RAFAEL MARTÍNEZ-GALARZA¹, EILEEN MEYER⁷*Submitted to ApJ*

ABSTRACT

To constrain the emission mechanisms responsible for generating the energy powering the active galactic nuclei (AGN) and their host galaxies, it is essential to disentangle the contributions from both as a function of wavelength. Here we introduce a state-of-the-art AGN radio-to-X-ray spectral energy distribution fitting model (ARXSED). ARXSED uses multiple components to replicate the emission from the AGN and their hosts. At radio wavelengths, ARXSED accounts for radiation from the radio structures (e.g., lobes, jets). At near-infrared to far-infrared wavelengths, ARXSED combines a clumpy medium and a homogeneous disk to account for the radiation from the torus. At the optical-UV and X-ray, ARXSED accounts for the emission from the accretion disk. An underlying component from radio to UV wavelengths accounts for the emission from the host galaxy. Here we present the results of ARXSED fits to the panchromatic SEDs of 20 radio-loud quasars from the 3CRR sample at $1 < z \lesssim 2$. We find that a single power-law is unable to fit the radio emission when compact radio structures (core, hot spots) are present. We find that the non-thermal emission from the quasars' radio structures contributes significantly ($> 70\%$) to the submm luminosity in half the sample, impacting the submm-based star formation rate estimates. We present the median intrinsic SED of the radio-loud quasars at $z > 1$ and find that the median SED of Elvis et al. (1994) is unable to describe the SED of the radio-selected AGN at $z > 1$. The AGN torus and accretion disk parameters inferred from our fitting technique agree with those in the literature for similar samples. We find that the orientation of the torus/accretion disk does not line up with the inclination of the radio jets in our sample.

Keywords: Quasars: Radio-Loud – AGN: high-redshift – SED: galaxies – galaxies: active – AGN: 3CRR

1. INTRODUCTION

It is now widely accepted that the center of every galaxy hosts a supermassive black hole (SMBH), which by accretion of gas and dust can turn into an active galactic nucleus (AGN; for a review see Heckman & Best 2014). While there has been significant progress in our understanding of galaxy formation and evolution in the past decades (e.g., Madau & Dickinson 2014), there is as yet no coherent picture of the role AGN play in this evolution (e.g., see Page et al. 2012; Aird et al. 2012; Rovilos et al. 2012; Rosario et al. 2012; Azadi et al. 2015; Bernhard et al. 2016; Brown et al. 2019; Shangguan et al. 2020). As they both release a tremendous amount of energy over a wide range of wavelengths, to better understand the emission mechanisms operating in the AGN and in the host galaxy and their inter-relationships, it is critical to disentangle the radia-

tion from both as a function of wavelength.

Emission from The Accretion Disk: In the standard picture of an active galaxy (e.g., Urry & Padovani 1995), the SMBH is surrounded by a gaseous accretion disk that generates the optical-X-ray emission (e.g., Novikov & Thorne 1973; Shakura & Sunyaev 1976; Rees 1984). The temperature and the optical depth of the gas in the disk are inversely related to the distance from the SMBH. The temperature gradient results in an energy gradient in the emission, with hard X-rays ($> 2\text{KeV}$) originating in the inner region while optical and UV radiation arises in the outer disk (e.g., Done et al. 2012; Kubota & Done 2018). The hard X-ray radiation is due to the Compton up-scattering of the accretion disk photons in a hot (electron temperatures $\sim 100\text{KeV}$) and optically thin corona that situated above and below the inner disk (e.g., Haardt & Maraschi 1993; Svensson & Zdziarski 1994; Petrucci et al. 2001). This hard X-ray emission is usually described with a simple power-law. At lower energies ($\sim 2\text{keV}$), many AGN show a soft excess over and above the extension of the harder power-law (e.g., Gierliński & Done 2004; Piconcelli et al. 2005; Bianchi et al. 2009). While there is no single, widely accepted origin for this excess (e.g., Crummy et al. 2006; Czerny et al. 2003; Petrucci et al. 2018) here we investigate the possibility that it results from Comptonization of thermal photons by a warm ($kT_e \sim 0.1\text{--}1\text{keV}$) optically thick ($\tau \sim 10\text{--}25$) layer above the surface of the disk, included in accretion disk

¹ Center for Astrophysics | Harvard & Smithsonian, 60 Garden Street, Cambridge, MA, 02138, USA

² European Southern Observatory, Karl-Schwarzschild-Str. 2, 85748 Garching b. München, Germany

³ H.H. Wills Physics Laboratory, University of Bristol, UK

⁴ Kapteyn Institute, University of Groningen, The Netherlands

⁵ Astronomisches Institut, Ruhr-University, Bochum, Germany

⁶ Steward Observatory, University of Arizona, 933 North Cherry Avenue, Tucson, AZ, 85721, USA

⁷ Department of Physics, University of Maryland Baltimore County, Baltimore, MD, 21250, USA

models (e.g., Czerny et al. 2003; Kubota & Done 2018; Petrucci et al. 2018). In these models, the UV and optical radiation originates from the outer regions of the disk. The total radiative power of the accretion disk depends on the black hole mass, the mass accretion rate, the spin of the SMBH, radial dependence of the optical depth (e.g., Davis & Laor 2011; Done et al. 2012; Kubota & Done 2018).

Emission from The Torus: The SMBH and the accretion disk are surrounded by an asymmetric dusty structure (the torus) which absorbs some of the UV and optical photons and re-radiates them at near-infrared (NIR) to MIR-infrared (MIR) wavelengths (e.g., Neugebauer et al. 1979; Rieke & Lebofsky 1981). Radiation from the torus dominates a quasar’s emission at 1–40 μm (e.g., Elvis et al. 1994; Netzer et al. 2007; Mullaney et al. 2011). The distribution of dust in the torus has been the subject of many studies. Early studies proposed a homogeneous structure in which the dust is smoothly distributed in a toroidal disk (e.g., Pier & Krolik 1992; Efstathiou & Rowan-Robinson 1995; Fritz et al. 2006). However, these models are not able to describe some of the observed features, for example the 9.7 μm silicate absorption feature in Type 1 sources (e.g., Roche et al. 1991). A significant part of the MIR radiation comes from the polar regions (e.g., Braatz et al. 1993; Hönig et al. 2013) which toroidal models could not explain. A clumpy circumnuclear torus was then put forward as a possible solution (e.g., Nenkova et al. 2008; Hönig & Kishimoto 2010; Hönig et al. 2013). Recently Siebenmorgen et al. (2015) proposed a model in which the dust can be distributed in a homogeneous disk, or a clumpy medium, or a combination of both (Siebenmorgen et al. 2005; Feltre et al. 2012). Models which combine both features successfully reproduce the MIR spectra of AGN, including the 9.7 μm silicate absorption feature in Type 1 AGN, the radiation from the hot dust close to the sublimation temperature, and the MIR radiation from the ionization cone (e.g., Braatz et al. 1993; Cameron et al. 1993; Hönig et al. 2013).

Emission from The Radio Structures: In addition to the X-ray to IR emission noted above, a subset of AGN ($\sim 15\%$, Kellermann et al. 1989; Urry & Padovani 1995) emit strongly at radio frequencies (for a recent review see Hardcastle & Croston 2020) as a result of the interactions of relativistic electrons (or protons) with the magnetic fields (see Ghisellini 2013, for a detailed review). These radio-loud AGN launch powerful jets which persist as highly collimated structures until they terminate as bright shocks (hot spots) at the interface with the circumgalactic or intergalactic medium. Radio-loud AGN are classified on the basis of their radio power, morphology, and radio spectral shape. They are designated as FR II or FR I depending on whether their radio power $P_{178\text{MHz}}$ is in excess of $10^{26.5} \text{ W Hz}^{-1} \text{ sr}^{-1}$ or not, respectively (Fanaroff & Riley 1974). FR II galaxies are double-lobed sources and their jets are brightest at the lobe edges. FR I galaxies’ jets are brightest in the centers of their lobes. The orientation of these AGN to the observer’s line of sight results in another classification as quasars and radio galaxies.

The observed shape of the radio spectra varies with the size of the radio structure (length of the radio jets),

the age of the electron population, our viewing angle, among many other factors. In a simplified picture the radio spectrum of a lobe-dominated AGN can be described with a power-law ($L_\nu \propto \nu^\alpha$). However, in AGN with compact radio structures such as radio cores and hot spots a superposition of various self-absorbed components make the shape of the spectrum more complex. Therefore, to model the radio emission multi-component models with different spectral indices are required. The radiation from these structures eventually breaks at high frequencies as a result of synchrotron radiation losses and terminates at a cutoff frequency due to a drop in the electron energy (e.g., Blandford & Königl 1979; Königl 1981).

What sparks the radio-loud phase in some AGN is still unknown and may be stochastic by nature. Some studies find that the triggering mechanism of the radio-loud phase is intrinsic to the AGN rather than the host galaxies or the environments (e.g., Kellermann et al. 2016; Coziol et al. 2017), while others find cold star-forming gas in galaxies (e.g., Janssen et al. 2012; Best & Heckman 2012), the brightness of the cluster and density of the environment they live in (e.g., Burns 1990; Best et al. 2007) increase the likelihood of hosting a radio-loud AGN. The prevalence of radio-loud AGN and the power of their radio emission (i.e., $L_{1.4\text{GHz}}$) correlates strongly with the intrinsic properties of the SMBH (e.g., SMBH mass, Best et al. 2005; Coziol et al. 2017). Radio-loud AGN, on average, have a higher Eddington ratio (which is the ratio of the bolometric luminosity to the Eddington luminosity)

$$\lambda_{\text{Edd}} = L_{\text{bol}}/L_{\text{Edd}}; \quad L_{\text{Edd}} \propto M_{\text{BH}} \quad (1)$$

bolometric luminosity and BH masses than their radio-quiet counterparts (e.g., Coziol et al. 2017). Such high accretion rates and radiative efficiencies occur relatively rarely, so the majority of the AGN population end up as radio-quiet or weak radio emitters.

The multiple components described above emit radiation covering 10 decades of frequency from X-ray to radio. To constrain these components we therefore need observations across a broad range of wavelengths. However, obtaining a multi-wavelength dataset is very challenging and in the case of quasars, variability adds more complications. Over the past three decades, numerous studies have focused on spectral energy distribution (SED) analysis of AGN populations (e.g., Edelson & Malkan 1986; Elvis et al. 1994; Richards et al. 2006; Shang et al. 2011; Elvis et al. 2012; Hao et al. 2014). A number of these studies attempt to understand whether quasars’ behavior can be described with an average SED. Elvis et al. (1994) presented the first high quality broad (X-ray to radio) atlas of quasar SEDs at $z \lesssim 1$ using then-current telescopes such as *Einstein*, the *International Ultraviolet Explorer (IUE)*, and Infrared Astronomical Satellite *IRAS*. Elvis et al. (1994) presented median SEDs for the radio-loud and radio-quiet quasars which have been extensively used and overall works remarkably well at 0.1–1 μm wavelength range for AGN of various luminosity and Eddington ratio (Elvis 2010). However, there is a large dispersion around their median SED which can reflect on the inferred properties of the quasars. Additionally, their sample is not representative of the overall quasar

population and is favored towards X-ray bright, and blue quasars (e.g., Jester 2005; Shang et al. 2011).

The average SED of quasars has been investigated by others in a similarly broad range of the spectrum (X-ray-radio) (e.g., Richards et al. 2006; Shang et al. 2011; Elvis et al. 2012) or a more limited range (e.g., Kuraszkiewicz et al. 2003; Polletta et al. 2007; Mullaney et al. 2011; Lani et al. 2017, among others) using more recent spectroscopic and photometric data. Richards et al. (2006) find a wide range of SED shapes for quasars and conclude that assuming an average SED can potentially lead up to 50% errors in the bolometric luminosities estimation. Hao et al. (2014) find that in X-ray selected, radio-quiet quasars the average SED has no significant dependence on redshift, bolometric luminosity, SMBH mass, and the Eddington ratio, while others find that local quasars templates may not be applicable to AGN at higher redshifts (e.g., Geach et al. 2011; Kirkpatrick et al. 2017). One of the many challenges in AGN SED analysis is the contamination of the broadband photometry by host galaxy. Most of the studies noted here use scaling relations such as $M_{BH} - \sigma$ (e.g., Hunt 2003) or $L_{host} - L_{AGN}$ (Vanden Berk et al. 2006) or color-color diagnostics (e.g., Grewing et al. 1968; Sandage 1971) to estimate the host galaxy contamination. However, each of these scaling relations has large uncertainties that significantly effect the SED analysis.

With the wealth of information stored in the photometric data obtained with modern telescopes with higher sensitivity and resolution, many studies have moved towards fitting complex models to the broadband photometry that can describe the radiation from the AGN and the host galaxy simultaneously and provide estimates of the physical properties of each (i.e. SMBH mass, stellar mass). The galaxy SED models (e.g., MAGPHYS: da Cunha et al. 2008; FAST: Kriek et al. 2009; CIGALE: Boquien et al. 2019) adopt libraries of galaxy templates with different stellar populations. These libraries are often built on assumptions on star formation history (SFH), initial mass function (IMF), dust attenuation law, etc which each have their own caveats and uncertainties. In the case of active galaxies, additional templates (i.e. torus, accretion disk) are required to describe the radiation from the central engine. For instance, Berta et al. (2013) presented SED3fit model which combines the galaxy templates from MAGPHYS SED model (da Cunha et al. 2008) with the torus templates of Fritz et al. (2006) to describe the radiation from the AGN and their hosts within $8 - 500 \mu m$. Leja et al. (2018) use the galaxy SED model of Prospector- α (Leja et al. 2017) and the clumpy torus model of Nenkova et al. (2008) to fit the SED of nearby AGN at $1-100 \mu m$ wavelength range. While overall, these models are successful in modeling AGN and the host galaxy's emission, portraying a complete picture of AGN requires dataset that in addition to the IR wavelengths, covers the radiation from the accretion disk which is the primary source of AGN power and the radio component (in the case of radio-loud AGN).

In this study we focus on SED modeling of a subset of AGN from the Revised-Third Cambridge Catalogue of Radio Source (3CR; Spinrad et al. 1985). We have com-

pared the full X-ray to radio SED of 3CRR⁸ (Laing et al. 1983) quasars and radio galaxies at $1 < z \lesssim 2$ and define an orientation-independent sample of luminous AGN. We particularly focus on this epoch as it harbors profound cosmological significance for the growth of SMBHs and the assembly of galaxy bulges in which they reside and was populated by powerful radio galaxies and quasars in numbers ~ 1000 times larger than at $z \approx 0$.

SED fitting of the full IR continuum of 3CR sources at a range of redshifts concludes that orientation determines the continuum shapes (e.g., Drouart et al. 2014; Podigachoski et al. 2015, 2016b). Here we expand on earlier SED fitting of the IR continuum to include the X-ray to radio emission. In this paper we introduce detailed, state-of-the-art AGN Radio-X-ray SED modeling (ARXSED) and focus on modeling the 3CRR quasars and analysis of the physical properties of the AGN components derived from our modeling (e.g., SMBH mass, Eddington ratio). SED fitting of the radio galaxies and an investigation of the relation between the AGN and their host galaxies will be presented in future papers.

This paper is organized as follows: Section 2 describes the sample selection and the multi-wavelength data used for the SED analysis. Section 3 presents the details of our SED modeling and the components used to describe the emission from the AGN and the host galaxy at different wavelengths. Section 4.1 describes the fitting results for individual sources and results of the SED analysis are discussed in Section 5. We present a summary of our findings in Section 6. Throughout the paper we adopt a flat cosmology with $\Omega_{\Lambda} = 0.7$ and $H_0 = 72 \text{ km s}^{-1} \text{ Mpc}^{-1}$.

2. SAMPLE AND DATA COMPILATION

The revised version of the 3CR catalog (3CRR) (Laing et al. 1983) includes 180 FR II radio galaxies and quasars up to redshift $z = 2.5$ and is 100% complete to a 178 MHz flux density of 10 Jy. AGN have obscuration-dependent emission that results in strong selection effects at most wavelengths (e.g., Azadi et al. 2017). However, low-frequency (178 MHz) radio emission uniquely finds all the AGN being dominated by synchrotron emission from optically-thin radio lobes. In a sequence of papers, we focus on SED analysis of a subset of 3CRR AGN at $1 < z \lesssim 2$ which includes 38 radio-loud AGN (21 quasars and 17 radio galaxies, Wilkes et al. 2013) and their host galaxies physical properties. We limit the analysis of this study to the 20 quasars from this sample. We have excluded the red quasar 3C 68.1 from this analysis as its SED is similar to those of the radio galaxies. Table 1 presents the objects in this sample along with their coordinates and redshifts.

The radio properties of our sample, from the radio morphologies and the length of the radio structures (e.g., radio jets measured from lobe to lobe), to the fraction of radiations from the radio core at 5 GHz, among many other properties have been studied in great detail (Akujor et al. 1991; Bridle et al. 1994; Akujor & Garrington 1995; Lonsdale & Barthel 1984; O'Dea 1998; Ludke et al. 1998, among many others).

Although the 3CRR sample has been extensively stud-

⁸ The Revised-3CR (3CRR) is a subset of 3CR sample that only includes extragalactic sources, with flux limit $> 10 \text{ Jy}$, DEC $> 10^\circ$ and Galactic latitude $> 10^\circ$ or $< -10^\circ$.

Table 1
The 3CRR quasars modeled in this work

Name	RA,DEC (J2000.0)	z
3C 009	00:20:25.2,+15:40:55	2.009
3C 014	00:36:06.5,+18:37:59	1.469
3C 043	01:29:59.8,+23:38:20	1.459
3C 181	07:28:10.3,+14:37:36	1.382
3C 186	07:44:17.4,+37:53:17	1.067
3C 190	08:01:33.5,+14:14:42	1.195
3C 191	08:04:47.9,+10:15:23	1.956
3C 204	08:37:44.9,+65:13:35	1.112
3C 205	08:39:06.4,+57:54:17	1.534
3C 208	08:53:08.8,+13:52:55	1.110
3C 212	08:58:41.5,+14:09:44	1.048
3C 245	10:42:44.6,+12:03:31	1.029
3C 268.4	12:09:13.6,+43:39:21	1.398
3C 270.1	12:20:33.9,+33:43:12	1.532
3C 287	13:30:37.7,+25:09:11	1.055
3C 318	15:20:5.40,+20:16:06	1.574
3C 325	15:49:58.4,+62:41:22	1.135
4C 16.49	17:34:42.6,+16:00:31	1.880
3C 432	21:22:46.2,+17:04:38	1.785
3C 454.0	22:51:34.7,+18:48:40	1.757

ied, surprisingly many sources miss critical data needed for estimating the basic parameters of their central engines and their host galaxies. For the SED analysis we have compiled the full X-ray to radio SED by combining archival data from *Chandra*, *XMM-Newton*, SDSS, UKIRT, 2MASS, *Spitzer*, *WISE*, *Herschel* and multi-frequency radio observations. The X-ray data used in this analysis is from Wilkes et al. (2013) and the optical and UV data are gathered from the references available on NASA/IPAC Extragalactic Database (NED). The NIR to FIR photometry used here is drawn from Podigachoski et al. (2015). Table 2 indicates the submm fluxes recently obtained from the SMA or ALMA for our analysis. Tables A1–A3 in appendix present the radio observations (with their references) used in our analysis.

We assembled the final SEDs from these datasets by selecting the highest-quality photometry. The photometry that significantly deviated from those within the same wavelength range due to variability were removed. We excluded photometry with $S/N < 3$ at any wavelengths except at FIR and submm wavelengths, where the upper limits are the only constraints available. Finally, we note that the UV-optical photometry is not contaminated by the emission lines. We fitted a power-law continuum in IRAF (Tody 1986) to regions of the spectrum that were uncontaminated by emission lines using continuum windows of Kuraszkiwicz et al. (2002). The power-law was then binned into 10–15 continuum bins and included in our SEDs.

3. SED COMPONENTS AND THE FITTING ROUTINE

One of the most important advantages of this study relative to previous work is that it accounts for emission over ten decades in frequency, from X-ray to radio wavelengths. Because both the AGN and host galaxies contribute throughout the electromagnetic spectrum, it is critical to disentangle the contributions from each as a function of wavelength in order to quantify the contributions of the various physical mechanisms to the overall energy budget. In this section, we first describe the components used in our SED model (ARXSED) to account for the AGN emission, and then describe the

Table 2
Recent submm data obtained with the SMA or ALMA

Name	ν (GHz)	Flux (mJy)	Telescope
3C 212 ¹	98	106 ± 5.3	ALMA
3C 212 ¹	233	41 ± 2.1	ALMA
3C 245 ²	224	84 ± 1	SMA
3C 270.1 ³	235	13.5 ± 0.3	SMA
3C 318 ⁴	315	2.3 ± 0.6	ALMA
3C 454.0 ⁴	315	10.6 ± 1.4	ALMA

- 1) PI: Meyer; Proposal ID: 2019.1.01709.S
- 2) PI: Ashby; Proposal ID: 2019B-S034
- 3) PI: Ashby; Proposal ID: 2019A-S031
- 4) PI: Podigachoski; Proposal ID: 2015.1.00754.S

component used to model the emission from the host galaxy. Additionally, we describe the methods used for correcting for the obscuration from the torus, the host galaxy, and the Milky Way absorption along the line of sight.

3.1. The AGN Components in ARXSED

Here we describe the models accounting for the AGN emission as arising from three components: an accretion disk, an obscuring torus, and radio lobes.

3.1.1. The Accretion Disk Component

For the accretion disk, we use the QSOSED model developed by Kubota & Done (2018). The primary variable parameters in this model are presented in Table 3. Below we describe the details of the model, the parameters in Table 3 and our technique for constructing the accretion disk templates using this model.

Kubota & Done (2018) assume that the emission from the accretion disk originates from three distinct regions: The inner region, extending from the innermost stable circular orbit (R_{ISCO}) to R_{hot} , the intermediate region extending from R_{hot} to R_{warm} , the outer region from R_{warm} to R_{out} . The R_{warm} and R_{hot} define the boundary of the hot and warm comptonization regions and R_{out} is the limit up to which the accretion disk extends (for more details see Appendix A of Kubota & Done 2018). The inner region with a temperature of ~ 100 KeV includes the hot corona with no underlying disk (i.e., a truncated disk). The plasma in this region emits the X-ray power-law component. In the intermediate region the warm comptonization occurs and the soft X-ray excess is produced. The electron temperature in this region is ~ 0.2 keV and the optical depth is $\sim 10-25$ (e.g., Czerny et al. 2003; Gierliński & Done 2004; Petrucci et al. 2013; Middei et al. 2018). The nature of the warm comptonization is not completely known (e.g., Done et al. 2012) and it may be a result of the failed UV-driven wind arising from the outer regions of the disk that falls back down into the disk (Laor & Davis 2014). The outer region of the disk is the standard optically thick accretion disk dominated by the blackbody emission.

The QSOSED model fixes the accretion disk parameters to typical AGN values of $kT_{e,hot} = 100$ keV, $kT_{e,warm} = 0.2$ keV, $\Gamma_{warm} = 2.5$, $R_{warm} = 2R_{hot}$, $R_{out} = R_{sg}$ which are respectively, the electron temperature for the hot and warm comptonization components and the spectral index of the warm comptonization component. The spectral index of the hot comptonization component, Γ_{hot} , is calculated via equation

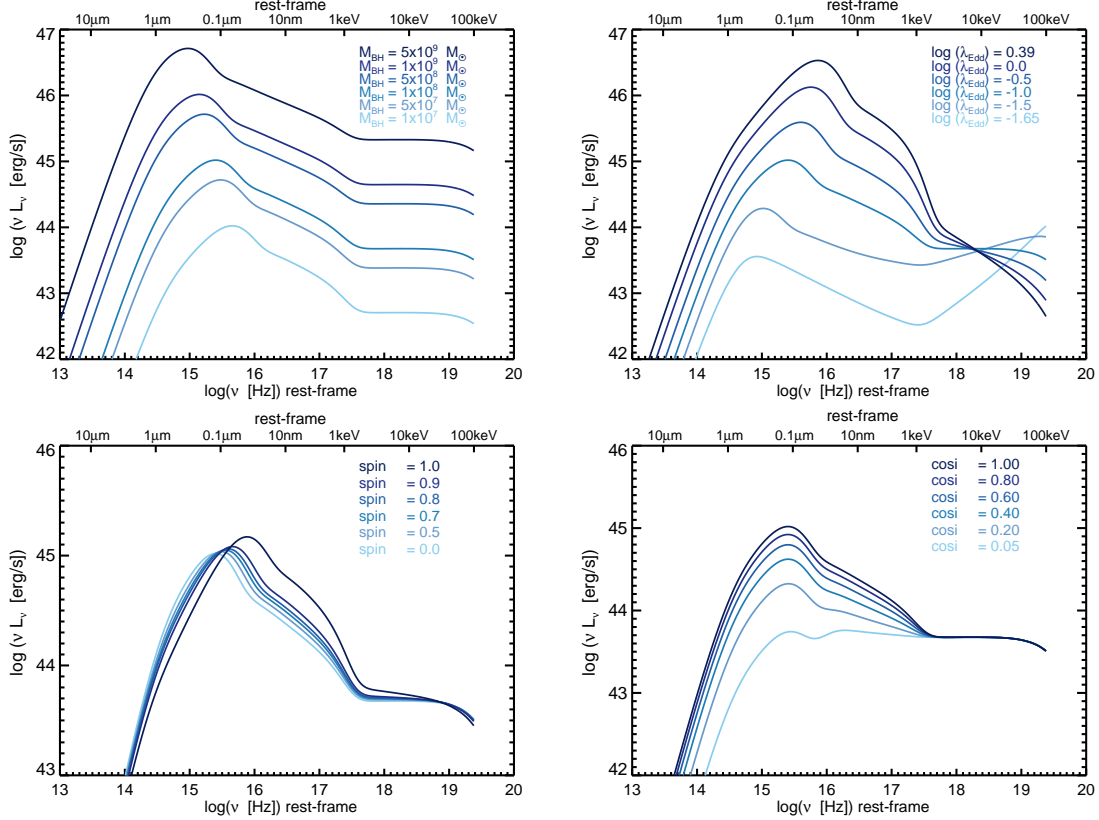


Figure 1. The effect of variation of each of the primary variable parameters in the QSOSSED model (Kubota & Done 2018) on the accretion disk SED while other parameters are kept constant. *Top-Left:* An increase in the BH mass results in a more luminous and cooler accretion disk. *Top-Right:* An increase in the mass accretion rate results in a more luminous and hotter accretion disk. *Bottom-Left:* An increase in the spin results in a more luminous and hotter accretion disk with higher radiative efficiency. *Bottom-Right:* An increase in the inclination angle from face-on to edge-on results in a more luminous optical-UV SED.

Table 3

The initial estimates, range of variation and steps used in constructing the accretion disk templates as well as the acceptable range for each parameter in the QSOSSED model

Parameter	Initial estimate	Range of variation	Steps	Acceptable range
$\log(M_{BH})$	M_0 (C IV or Mg II)	$[\log(M_0)-1, \log(M_0)+1]$	0.2 dex	[7,10]
$\log(\lambda_{Edd})$	—	$[-1.65, 0.39]$	0.2 dex	$[-1.65, 0.39]$
spin (a)	—	$[0.75, 0.998]$	0.02	$[0, 0.998]$
inclination angle (θ_D)	θ_T	$[\theta_T-12, \theta_T+12]$	θ_T dependent	[0,90]

6 in Kubota & Done (2018). As described above, the R_{warm} and R_{hot} define the boundary of the hot and warm comptonization regions (for more details see Appendix A of Kubota & Done 2018) and R_{sg} is the self-gravity radius (see equation 4 of King 2016). The QSOSSED model includes reprocessed radiation which is the fraction of the hot comptonization component that illuminates the warm comptonized material and cool outer disk (which has a temperature of a few thousands of kelvin).

The primary variable parameters in the QSOSSED model are the supermassive black hole mass M_{BH} , the rate of accretion ($\log \dot{m}$, which is the Eddington ratio in log space, see equation 1), the inclination angle and the dimensionless spin parameter $a \equiv Jc/GM_{BH}^2$ where J is the angular momentum of the BH. Figure 1 illustrates the effect that variation of each parameter has on the shape of the optical, UV and X-ray synthetic spectra while keeping the other parameters constant. Overall, the effect of varying these parameters on the geometry

of the accretion disk and on its SED are intertwined. The top-left panel illustrates how an increase in the BH mass, while $\log \dot{m}$, and other parameters are constant results in a more luminous and cooler accretion disk. The top-right panel indicates that an increase in the Eddington ratio results in a more luminous and hotter accretion disk. Increasing the spin (bottom-left) can impact the geometry by moving the R_{ISCO} closer to the SMBH and the shape of the SED by moving the peak towards higher energies (similar to the Eddington ratio) and increase the radiative efficiency. The bottom-right panel of Figure illustrates, while all other parameters are kept constant, a face-on observer sees more of the UV bump compared to an edge-on observer.

To fit the optical-Xray SED of each quasar, we construct a set of QSOSSED templates in XSPEC⁹ covering a range for each parameter and using prior information

⁹ XSPEC is an interactive program used to fit models to energy spectra from optical to gamma-rays. For more information see <https://heasarc.gsfc.nasa.gov/xanadu/xspec/>

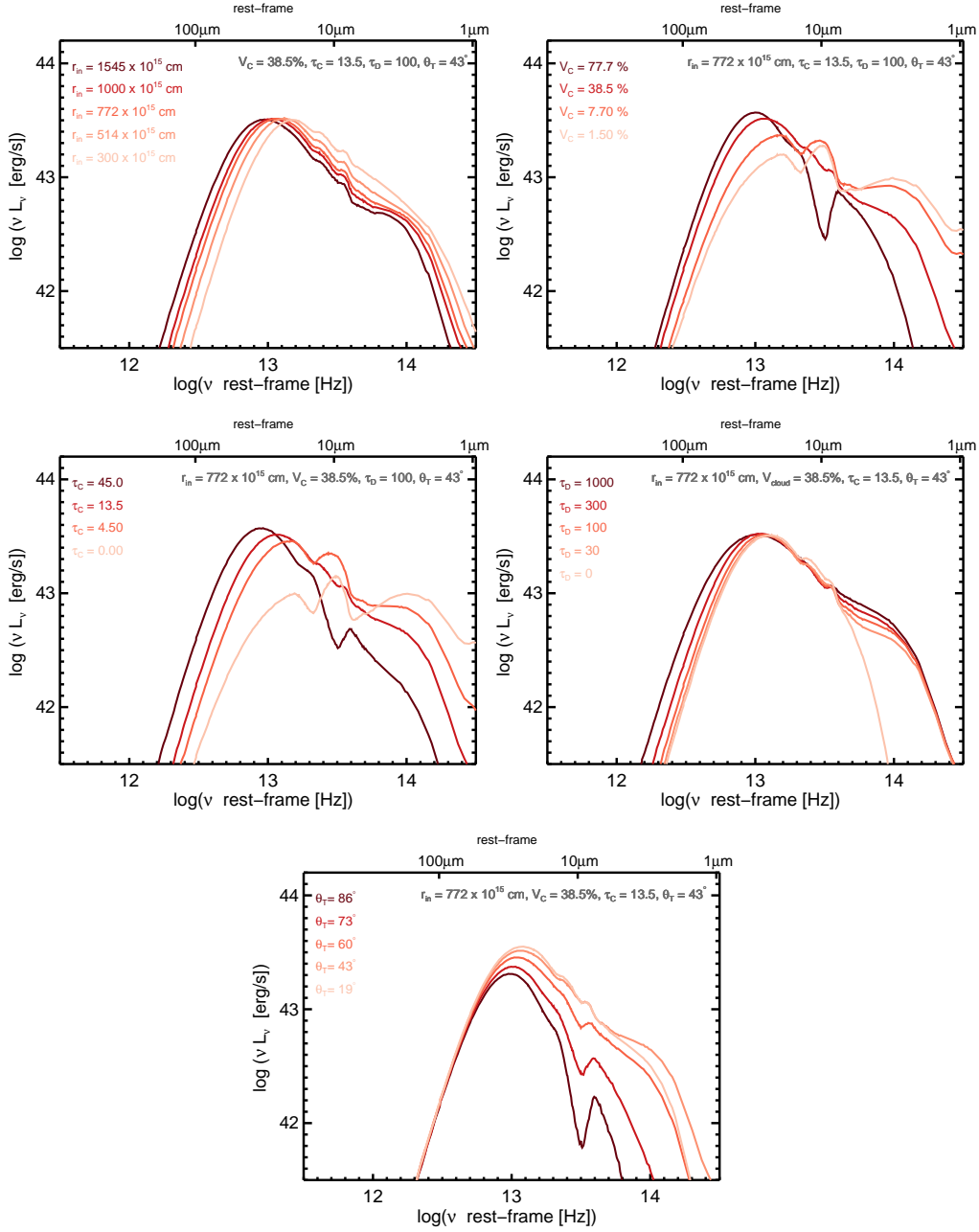


Figure 2. The impact of variation of one parameter on the torus SED while keeping the other parameters constant. *Top-Left:* As r_{in} increases the torus moves away from the central engine, thus the emission shortward of 10 μm decreases, and the peak of the torus emission moves to higher wavelengths. *Top-Right, Middle-Left:* As V_C and/or τ_C increase the higher density of clumps at radii close to the central engine results in more absorption so the silicate feature changes from emission to absorption. *Middle-Right:* An increase in τ_D results in more scattering from the disk surface at all radii, therefore results in more emission shortward and longward of 10 μm . *Bottom:* A change in the inclination angle from face-on to edge-on results in less pronounced emission shortward of 10 μm and change of the silicate emission feature to absorption.

when it is available as starting points for the templates. To construct the templates for each quasar we vary each parameter with a fixed step within their acceptable range in QSOSED. Table 3 summarizes the initial estimates, range of variation and steps used in our procedure and the acceptable range for each parameter in the model.

Out of 20 sources in our sample, 6 (3C 9, 3C 191, 3C 205, 3C 270.1, 3C 432, 3C 454.0) have broad C IV $\lambda 1548$ line and 6 (3C 14, 3C 181, 3C 186, 3C 204, 3C 245, 3C 268.4) have Mg II $\lambda 2800$ line available (obtained from SDSS archive, private communication or

Barthel et al. 1990) which we use to estimate the BH masses. For the remaining quasars without spectroscopic information, we use the median BH mass of the 12 sources with C IV or Mg II lines as the initial mass estimate. We note that BH mass measurements based on the high ionization C IV line have larger errors than those estimated from the Mg II or Balmer lines (e.g., Sulentic et al. 2002; Baskin & Laor 2005; Shen 2013). However, we only use this mass as initial estimate for making the accretion disk templates. We allow M_{BH} to vary within ± 1 dex around the initial mass estimates

Table 4
The free parameters and their acceptable values in Siebenmorgen et al. (2015) torus library

Parameter	Acceptable values
Inner radius ¹ (r_{in})	300, 514, 772, 1000, 1545 ($\times 10^{15}$ cm)
Cloud volume filling factor (V_C)	1.5, 7.7, 38.5, 77.7 (%)
Cloud optical depth (τ_C)	0, 4.5, 13.5, 45
Disk optical depth (τ_D)	0, 30, 100, 300, 1000
inclination angle (θ_T)	19, 33, 43, 52, 60, 67, 73, 80, 86 ($^\circ$)

1. The inner radius is the dust sublimation radius and scales with the total AGN luminosity as $R_{in} \propto L_{AGN}^2$. The values listed here are for an AGN of a luminosity of $10^{11} L_\odot$

in steps of 0.2 dex. Since there is no prior information on $\log \dot{m}$ we allow it to vary over the entire acceptable range in QSOSED in steps of 0.2 dex. The quasars in our sources are all radio-loud thus are expected to have high spin values (see Reynolds 2019, and references therein). Therefore we use a limited range from 0.75 to 0.998 in steps of 0.02 for spin. For the inclination angle, we use the best-fit value from the torus model (Section 3.1.2) then construct the templates by varying the inclination angle within $\pm 12^\circ$ of the initial estimate. However, rather than using a fixed step size we determine 7 values within $\pm 12^\circ$ of the initial estimate empirically. Overall, with this approach, we construct ~ 11000 templates to fit the optical-Xray SED of each quasar.

3.1.2. The Torus Component

Here we adopt the two-phase AGN torus model developed by Siebenmorgen et al. (2015) which assumes the dust around the AGN can be described as a clumpy medium or a homogeneous disk, or as a combination of both. Table 4 lists the primary variable parameters and their acceptable values in the model. Below we describe the details of the model, the variable parameters.

In Siebenmorgen et al. (2015) the inner radius (R_{in}) of the dusty structure is defined by the sublimation temperature of the dust grains. The outer radius of the structure is chosen to be $R_{out} = R_{in} \times 170$ which is large enough to have negligible impact on the observed features in the SED. The density of the dust decreases with radius. The dust grains are fluffy mixtures of silicate and amorphous carbon grains (Krügel & Siebenmorgen 1994) instead of the interstellar medium (ISM) dust grains (e.g., Siebenmorgen et al. 2014). These fluffy grains are more efficient absorbers and have higher submm emissivities than the diffuse ISM grains (for more details see Section 2.6 in Siebenmorgen et al. 2015).

The free parameters of the torus model, R_{in} , the optical depth of the homogeneous disk mid-plane (τ_D), the optical depth of the clumps (τ_C), the volume filling factor (V_C) and the inclination angle (θ_T) and their accepted values are listed in Table 4. Varying these parameters within their acceptable range makes a library with 3600 templates. We note that these templates are built for an AGN of luminosity $10^{11} L_\odot$. However, the SEDs are scale-invariant so the actual inner radius scales with luminosity of the primary source (i.e., the accretion disk) (e.g., Suganuma et al. 2006; Kishimoto et al. 2011):

$$R_{in} \propto L_{AGN}^2 \quad (2)$$

Figure 2 illustrates the effect that variation of each the parameter on the shape of the NIR-FIR SED, while keeping the other parameters constant. As R_{in} increases

the torus moves farther from the central engine (top-left panel) therefore the emission hotter dust grains become less pronounced and the peak of the torus SED moves to longer wavelengths. The impact of variation of the filling factor and optical depth of the clumps (top-right and middle-left) is intertwined. An increase in V_C and/or τ_C while the inclination angle and R_{in} are constant changes the SED from one with a silicate emission feature at $9.7 \mu\text{m}$ to a one with an absorption feature. In fact an increase in V_C and/or τ_C when the homogeneous disk is unchanged result in more absorption at shorter wavelengths (because of a higher density of the clouds closer to the central engine) and the peak of the torus emission moves to higher wavelengths. An increase in the opacity of the homogeneous disk (τ_D) results in more scattering from the disk surface which acts similarly to adding more hot and cold dust grains (for a face-on observer). Therefore the emission from short and long wavelengths both increases. We note that this will not be the same for an edge-on observer (see Figures 4 and 5 in Siebenmorgen et al. 2015) As the observer's inclination angle changes from face-on towards edge-on (bottom panel), the observer sees less of the emission from the inner parts of the torus (short wavelengths) and rather than a silicate emission feature sees an absorption feature. We note in our fitting procedure in general we do not have any prior information to limit the torus parameters but see Section 4.1 for a few cases where the observed silicate feature helped to constrain the torus model.

As noted in the Introduction the MIR emission from the torus comes from the absorbed and reprocessed UV and optical photons radiated by accretion disk. Therefore, the SED shape of the primary source of emission might influence the reprocessed MIR radiation. The primary source of radiation in Siebenmorgen et al. (2015) is the Rowan-Robinson (1995) model, which describes the optical-UV continua of quasars with a broken power-law function. As noted in Section 3.1.1 we use the Kubota & Done (2018) accretion disk model. We examined the impact of various accretion disk models (including a simple blackbody, Kubota & Done 2018 and a few others) on the torus SED, and found that the SED shape longward of $1 \mu\text{m}$ (rest-frame) is independent of the chosen accretion disk template at wavelengths shorter than $1 \mu\text{m}$.

3.1.3. The Radio Component

In this section we describe the four models developed in our study to model the radiation from quasars' radio structures. To constrain the radio fits parameters and to understand which of the four models better describe the radio emission we use the radio properties listed in Ta-

Table 5
Radio properties of the quasars in our sample

Name	Type ¹	R_{CD}^2	Projected jets length ³ (kpc)	Inclination angle ⁴ (°)	De-projected jets length ⁵ (kpc)	Range of de-projected jets length ⁶ (kpc)
3C 009	-	0.009	85	52 ± 10	151	[135,178]
3C 014	-	0.018	213	42 ± 10	308	[261,389]
3C 043	CSS	< 0.060	26	> 26	< 49	-
3C 181	-	0.009	59	49 ± 10	65	[57,77]
3C 186	CSS	0.042	16	42 ± 10	20	[17,25]
3C 190	CSS	0.098	25	27 ± 10	124	[94,194]
3C 191	-	0.102	34	31 ± 10	81	[64,116]
3C 204	-	0.087	296	34 ± 10	543	[437,748]
3C 205	-	0.0309	154	38 ± 10	251	[208,330]
3C 208	-	0.105	107	32 ± 10	172	[136,243]
3C 212	-	0.204	73	20 ± 10	216	[147,425]
3C 245	-	1.950	40	4^{+10}_{-4}	1067	[307,-]
3C 268.4	-	0.091	85	27 ± 10	205	[155,319]
3C 270.1	-	0.282	103	16 ± 10	374	[235,987]
3C 287	CSS	$< 0.102^7$	8	-	-	-
3C 318	CSS	< 0.138	9	58 ± 10	8	[7,9]
3C 325	-	0.003	124	-	-	-
4C 16.49	-	0.052	145	39 ± 10	216	[180,281]
3C 432	-	0.025	111	46 ± 10	155	[134,190]
3C 454.0	CSS	< 0.339	10	> 14	< 46	-

1) Compact Steep Spectrum (Wilkes et al. 2013)

2) Radio core dominance (see equation 3)

3) Projected radio sizes, measured lobe-to-lobe from high resolution images at 5Hz

4) Jets inclination angle (Marin & Antonucci 2016)

5) De-projected radio sizes, measured lobe-to-lobe at 178 MHz

6) The range of the de-projected sizes estimated from the errors on the inclination angles

7) We did not find the R_{CD} estimate for 3C 287 in the literature, so we adopted the average values of the other CSS quasars as an upper limit.

ble 5. The first column of the table gives the source name, second column indicates whether the quasar is classified as a compact steep spectrum (CSS) source, third column lists the radio core dominance parameter (Orr & Browne 1982), i.e., the ratio of radio-core to extended radio-lobe emission, both measured at 5 GHz:

$$R_{CD} = L_{core}(5\text{ GHz})/L_{lobe}(5\text{ GHz}) \quad (3)$$

from (Wilkes et al. 2013). The fourth column gives the projected radio jet length measured lobe-to-lobe at 178 MHz taken from the compilation of C. Willott¹⁰. The fifth column lists the radio jets inclination angle, accurate to within $\pm 10^\circ$ from Marin & Antonucci (2016) (estimated from the radio core fractions – see their Section 3). The de-projected radio jet lengths (listed in sixth column) were calculated using the projected jet sizes and dividing them by the sine of the jets inclination angle. The last column indicates the range of the de-projected jets length taking into account the errors on the jet inclination angle.

To fit the radio emission from the quasars in our sample we start by considering a relativistic electron population with a power-law energy distribution in a magnetic field of B :

$$N(E) \propto E^{-p} \quad (4)$$

Synchrotron emission is generated by these relativistic electrons spiraling around magnetic field lines. Although synchrotron radiation is absorbed by the electrons in optically thick regions (synchrotron self-absorption), radio photons from optically thin regions reach the observer. We can formulate synchrotron emission transitioning from an optically thick, self-absorbed region to

an optically thin region with the radiative transfer equation (for more details see Section 4.4–4.7 in Ghisellini 2013):

$$I(\nu) = \frac{\epsilon(\nu)}{\kappa_\nu} (1 - e^{-\tau_\nu}); \quad \tau_\nu \equiv R\kappa_\nu \quad (5)$$

in which τ_ν is the spectral optical depth, R is the size of the emitting region. $\epsilon(\nu)$ is the emissivity, and κ_ν is the specific absorption coefficient and are described as

$$\epsilon(\nu) \propto B^{(p+1)/2} \nu^{-(p-1)/2} \quad (6)$$

$$\kappa_\nu \propto B^{(p+2)/2} \nu^{-(p+4)/2}. \quad (7)$$

In a self-absorbed regime $\tau_\nu \gg 1$, therefore the second component in the radiative transfer equation becomes negligible and equation 5 can be simplified (see Section 4.5 in Ghisellini 2013) to:

$$I(\nu) = I_0(\nu) \propto B^{-1/2} \nu^{5/2} \quad (8)$$

Setting ν_t to be the frequency at which the a transition from optically thick to thin occurs, then

$$\tau_{\nu_t} \equiv R\kappa_{\nu_t} = 1 \quad (9)$$

and using equation 7 we then obtain

$$\nu_t \propto [RB^{(p+2)/2}]^{2/(p+4)} \quad (10)$$

therefore

$$\tau_\nu \equiv R\kappa_\nu = \left(\frac{\nu_t}{\nu}\right)^{(p+4)/2} = \left(\frac{\nu_t}{\nu}\right)^{(p-1)/2+5/2} \quad (11)$$

¹⁰ <http://astroherzberg.org/people/chris-willott/research/3crr/>

Now if we consider $\alpha_2 = -(p-1)/2$ as the spectral index in the optically thin region and $\alpha_1 = 5/2$ as the spectral index in the optically thick region we can rewrite equation 5 as

$$I(\nu) \propto \left(\frac{\nu}{\nu_t}\right)^{\alpha_1} [1 - \exp(-(\frac{\nu_t}{\nu})^{\alpha_1 - \alpha_2})] \quad (12)$$

However, as the electron population ages it loses its energy and eventually the synchrotron radiation terminates at a cutoff frequency. Therefore an additional term is required to account for this energy loss (Polletta et al. 2000):

$$L_\nu \propto \left(\frac{\nu}{\nu_t}\right)^{\alpha_1} [1 - \exp(-(\frac{\nu_t}{\nu})^{\alpha_1 - \alpha_2})] e^{-\frac{\nu}{\nu_{\text{cutoff}}}} \quad (13)$$

Equation 13 describes radiation from both optically thick and thin regions which terminates at high energies due to energy loss. This equation is based on many assumptions including, the charged particle is an electron, the electron population's energy has a power-law distribution, the minimum energy condition between the relativistic particles and the magnetic field is met, the source is homogeneous and therefore $\alpha_1 = 2.5$. In order to describe the radio emission from the quasars in our sample, we use the general form presented in equation 13 and modify it based on different conditions.

Model 1—A Single Power-Law with an Exponential Cutoff: In our first model we consider an AGN in which the radio emission is dominated by radiation from the optically thin lobes. In this case, a power-law can successfully describe the radio emission (Polletta et al. 2000):

$$L_\nu \propto \left(\frac{\nu}{\nu_{\text{cutoff}}}\right)^{\alpha_2} e^{-\frac{\nu}{\nu_{\text{cutoff}}}} \quad (14)$$

Model 2—A Double Power-Law with an Exponential Cutoff: The added presence of compact structures such as radio cores and hot spots may cause the spectral shape to deviate from a single power law. Therefore, in our second model, we assume a double power-law similar to Eq. 13. However, in our model, α_1 is a free parameter and is not fixed at 2.5 (since we do not expect a single, homogeneous component) and ν_t is the transition frequency from α_1 to α_2 dominated regions. As we discuss in Section 4.1 indeed some of the sources in our sample with bright hot spots can not be fitted with a single power-law and require a second component with a different spectral slope.

Model 3—A Parabola with a Cutoff: Relaxing the homogeneous assumption, in our third model instead of a broken power-law we assume a parabolic function which approximates a superposition of multiple power-law components some optically thick and some thin (Cleary et al. 2007):

$$\log L_\nu \propto -\beta(\log \nu - \log \nu_t)^2 + \log(e^{-\frac{\nu}{\nu_{\text{cutoff}}}}) \quad (15)$$

β in this equation indicates the curvature of the parabola.

Overall, Eqs. 13 or 15 can successfully describe the emission from a source with a mix of optically thick and thin regions (e.g., a lobe-dominated quasar with bright hot spots or a moderately bright core).

Model 4—A Parabola with a Cutoff & A Double Power-Law with an Exponential Cutoff: In quasars with bright cores, the superposed self-absorbed components may generate spectral shapes not amenable to fitting with these simple models. Therefore, in our fourth model we consider a combination of Eqs. 13 and 15, where Eq. 13 is solely used to describe the radio core emission, and Eq. 15 describes radiation from the lobes/hot spots. We note that in this case, the core and lobe components each have their own cutoff frequency.

We fit these four models to the observed radio photometry using the MPFIT nonlinear least-square fitting function in IDL (Markwardt 2009). The spectral slopes α_1 and α_2 in each model as well as β and ν_t are free parameters, and the cutoff frequency is limited to $10^{10} < \nu_{\text{cutoff}} < 10^{14}$ Hz.

3.2. The Host Galaxy Component

In this study we use the MAGPHYS SED code (da Cunha et al. 2008, 2015) to account for the contribution from the host galaxy. MAGPHYS is a widely used galaxy SED code capable of accounting simultaneously for different levels of star formation activity, stellar populations, dust obscuration, and star formation histories for galaxies at different redshifts. We did not use MAGPHYS to model AGN emission in our sources, because we handled that as described in Section 3.1.

MAGPHYS is built upon the energy balance technique, which links the UV and optical emission from the young stellar population to the IR emission from dust. In other words, starlight is the only source of dust heating and the energy absorbed by dust is equal to the re-radiated energy, and therefore no energy transfer is involved. The stellar emission from UV to NIR wavelengths is produced using the Bruzual & Charlot (2003) spectral population synthesis model (assuming a Chabrier 2003, IMF) attenuated by dust following Charlot & Fall (2000). The model assumes the young stars form in dense clouds (i.e., giant molecular clouds); when younger their emission is attenuated by the dust in their birth cloud and the ambient ISM, but as they age the birth clouds disappear on a time-scale of 10^7 yr, and the stellar emission is then absorbed only by the diffuse ISM (Charlot & Fall 2000). MAGPHYS considers four dust components, each including grains with a different size and temperature: polycyclic aromatic hydrocarbons (PAHs) grains, hot grains with temperatures in the range 130–250 K, grains in thermal equilibrium with temperature of 30–60 K, and cold dust grains with adjustable equilibrium temperature in the range 15–25 K. The stellar birth clouds contain the first three dust components and cold dust only exists in the ambient ISM. For more details, refer to da Cunha et al. (2008).

Although the original da Cunha et al. (2008) MAGPHYS code covers a broad wavelength range from 912 Å to 1 mm, here we use the updated da Cunha et al. (2015) version, which includes the galaxy contribution at radio wavelengths (for more details see Section 3.2 in da Cunha et al. 2015). In addition to broader wavelength coverage, da Cunha et al. (2015) includes a continuous delayed exponential SFH:

$$\Psi(t) \propto \gamma^2 t \exp(-\gamma t) \quad (16)$$

in which t is the time since the onset of star formation and $\gamma = 1/\tau_{SF}$ is the inverse of the star formation time scale (see Lee et al. 2010; da Cunha et al. 2015). da Cunha et al. (2015) also include absorption by the intergalactic medium (IGM) which can strongly impact the UV emission in high-redshift galaxies such as the ones treated here.

Although the da Cunha et al. (2015) model includes galaxy emission at radio wavelengths, the radio emission (both thermal and non-thermal components) in galaxies is ~ 4 –5 orders of magnitude lower than that in radio-loud AGN. Therefore AGN are the dominant sources of radio emission in the present analysis.

3.3. Dereddening and Absorption Corrections

In order to obtain the intrinsic SED of the AGN in our sample, it is necessary to correct the photometry for the reddening and absorption occurring at various wavelengths. In brief, these corrections include, correcting the X-ray observations for the host galaxy and the Milky Way absorption, correcting the UV–NIR photometry for the Milky Way absorption, and correcting the optical–UV radiation from the accretion disk for the dusty torus absorption.

X-ray photons are absorbed by the gas in their host galaxies (i.e., intrinsic) and along the line of sight in the Milky Way. In this study we adopt the best estimates of the intrinsic X-ray luminosity from Wilkes et al. (2013), i.e., corrected for both intrinsic and Galactic absorption. Additionally, we correct the UV–NIR (0.91 – 13.0 μm) photometry for absorption by the Milky Way using the attenuation law of $\tau_\lambda \propto \lambda^{-0.7}$ from Charlot & Fall (2000).

To estimate the extinction of the accretion disk emission from the obscuring structure in the torus we use the method of Siebenmorgen et al. (2015, see also Krügel 2009). According to this method the effective optical depth for any templates (with any combination of dust clouds and homogeneous disk) can be obtained via a comparison to the same template in the absence of dust (see Section 2.7 in Siebenmorgen et al. 2015):

$$\tau_{eff} = -\ln \frac{Flux_{template}}{Flux_{nodust}} \quad (17)$$

Thus, we first determine the template from Siebenmorgen et al. (2015) which best fits the NIR–FIR data corresponding to the AGN emission (not the host galaxy, see Section 3.4 for more details) and then apply equation 17 to estimate the effective optical depth. The UV and optical photometry (corresponding to the accretion disk emission) is then corrected by a factor of $e^{\tau_{eff}}$ for the absorption in the torus. We note that, depending on the best-fit, torus template τ_{eff} may be a negative or positive number indicating scattering or absorption by the dust structure. An edge-on observer is not able to see the scattered light from the torus and is mainly affected by absorption, i.e., a positive τ_{eff} , while a face-on observer sees the scattered light from the torus and is not affected by absorption, i.e., a negative τ_{eff} (see Siebenmorgen et al. 2015).

3.4. Fitting Methodology

In this Section we describe our fitting methodology and the steps in which the various attenuation and absorption correction from Section 3.4 are applied. The X-ray luminosities used in the fitting analysis are corrected for both intrinsic and the Milky Way absorption (Wilkes et al. 2013). We correct the X-ray emission in advance for the gas absorption since we have no independent way to estimate this beyond the X-ray data. Additionally, the photometry at UV–NIR wavelengths are corrected for the Milky Way absorption (see Section 3.3).

Given that our sample consists of radio-loud quasars, AGN emission dominates that of the host galaxy over most of the SED. Therefore, we allow the contribution of the AGN to the photometry to vary from 95% to 65% (in bins of 5%) at submm to UV wavelengths (at radio and X-ray wavelengths the host galaxy contribution is orders of magnitude smaller than the AGN). The AGN components dominating at submm to UV wavelengths, torus and accretion disk, are allowed to vary independently from each other. The range of normalization of the contribution of the AGN components results in an iterative process in which the steps below are followed:

Step 1: We start the fitting procedure by determining the template from Siebenmorgen et al. (2015) which best fits the photometry associated with the AGN at NIR–FIR wavelengths. Siebenmorgen et al.’s templates are normalized to a primary AGN of the luminosity of $10^{11} L_\odot$ (Section 3.1.2). Therefore to fit our quasars, we integrate the AGN luminosity within the range of 2–45 μm in rest-frame (at which wavelengths the torus is the dominant radiation source) and normalize the torus templates according to this integrated luminosity. We determine the best-fit torus using χ^2 minimization.

Step 2: We correct the optical–UV photometry associated with the accretion disk for the torus reddening implementing the correction factor obtained from equation 17. To do this we assume the line-of-sight to the accretion disk is the same as that for the torus. Considering that AGN are known to vary and the fact that some of sources are missing UV photometry, the accretion disks templates are normalized to the average flux in the 0.2–0.9 μm (rest-frame) band. We identify the best-fit accretion disk template via χ^2 minimization.

Step 3: We fit the radio photometry with the four models described in Section 3.1.3, and determine the best-fit using χ^2 minimization. We normalize the radio models to the 5 GHz photometry. In the fourth radio model, we use the 5 GHz core flux to normalize the core component and the remaining flux to normalize the parabola component. For the radio models, we inspected the radio images in several bands (178 MHz, 5 GHz, 8 GHz, and 15 GHz, if available) to reconcile multi-component models with different spectral indices are required with the presence of bright hot spots and/or cores emission.

Step 4: We subtract the best-fit AGN component (radio, torus and accretion disk) from the total observed photometry and fit this residual with MAGPHYS to account for the host galaxy contribution. To include the upper limits in MAGPHYS we follow the prescription of da Cunha et al. (2015) in which the flux densities are set to zero and the upper limit values are set as the flux uncertainty.

Step 5: We find the total fit by combining the AGN

and the host galaxy component.

Step 6: We repeat the steps 1–5 above for all the combinations of the torus and the accretion disk (95%-65%). We identify the best-fit as the one that not only results in one of the lowest χ^2 values for the total fit but also one of the lowest χ^2 values for individual components.

We note that after identifying the best-fit torus model - via χ^2 minimization- we examine the impact of variation of the torus parameters on the optical-UV SED and the total fit. This is particularly important for the so-called “red quasars” in our sample. This class of AGN are reddened Type 1 AGN in which the optical-UV SED lacks the big blue bump and which also have red MIR colors (e.g., Benn et al. 1998; Cutri et al. 2001; Lacy et al. 2004; Georgakakis et al. 2009; Kim & Im 2018). Understanding the nature of red quasars is beyond the scope of this paper. However, we assume that the reddening is due to obscuration, and to obtain a reasonable UV bump in these sources, we carefully examine the dependence of the shape of the intrinsic optical-UV SED on the torus parameters.

4. RADIO-TO-X-RAY SED ANALYSIS OF THE 3CRR QUASARS AT $1 < z \lesssim 2$

We present the SED analysis of the 3CRR quasars using the components described above (Section 3). We first describe the details of the best-fit AGN model for individual sources and then summarize the commonalities among sources.

4.1. Fitting Results for Individual Sources

The parameters for the best-fit accretion disk and torus and radio models are given in Tables 6 and 7. The errors on the accretion disk parameters in Table 6 are from the quantization steps used in constructing the accretion disk library (see Section 3.1.1). Figure 3 shows the full suite of photometry together with the best-fit models. The gray data points are the absorption corrected broadband photometry, and the black plus signs in optical-UV bands indicate the photometric points before the torus obscuration correction. The components in these plots are: radio component from the core, jets and lobes (light blue), infrared emission from the torus that contributes at rest-frame wavelengths longward $1 \mu\text{m}$ (dark red), the accretion disk component that accounts for the thermal optical to X-ray emission (green), the host galaxy component obtained from MAGPHYS SED fitting code (magenta) and the total fit (orange). The dark blue star indicates the core contribution to the 5 GHz photometry estimated from the R_{CD} presented in Table 5. The SED fits are presented in 3CRR number order below:

–**3C 9** has a jet of ~ 151 kpc (as noted in Section 3.1.3 de-projected length, measured lobe to lobe) and a core contribution of less than 1% at 5 GHz. The radio emission in this source is best described as a broken power-law (with an exponential cutoff at submm wavelengths, see Table 7) which is consistent with the presence of multiple features (i.e., jet, counter jet, bright hot spots based on 4.9 GHz VLA data, Bridle et al. 1994).

The emission from the torus is best described with a combination of clumps with negligible opacity and a homogeneous disk with the highest allowed optical depth (see Table 4). The filling factor and optical depth of the clumps indicate that there is not much obscuration

from the dust clouds along the line of sight. Therefore, a comparison of the gray squares with the black plus signs indicates the correction of the optical-UV emission from the torus obscuration is negligible. As noted in Section 3.1.1 the accretion disk templates are built within the range of $\pm 12^\circ$ from the inclination angle of the best-fit torus model. For this object, the inclination angle from the best-fit torus model is 52° while from the best-fit accretion disk template is 63° .

The accretion disk template lies below the X-ray data which suggests the presence of a non-thermal X-ray component. *Chandra* observations Fabian et al. (2003) find extended X-ray emission on both sides of the nucleus of 3C 9 coincident with the radio structure suggesting it is probably due to non-thermal inverse Compton emission from the interaction of the relativistic electrons with the cosmic microwave background. We note that this extended emission does not effect the nuclear X-ray emission used in our SED modeling.

–**3C 14** is a red quasars (Smith & Spinrad 1980) with less than 2% core contribution at 5 GHz and an extended radio jet of 308 kpc. The radio emission is best described with a broken power-law with an exponential cutoff at FIR wavelengths, consistent with the multiple radio structures present in MERLIN 18 cm data (Akujor et al. 1994). The SED fitting shows that the non-thermal emission contribution at submm/FIR wavelengths is negligible.

The emission from the torus is best described with a combination of clumps with negligible opacity, a homogeneous disk with moderate optical depth and inclination angle of 67° that result in moderate obscuration of the optical-UV emission. The optical-UV SED before obscuration correction (shown in black plus signs) is consistent with its classification as a red quasar. As noted in Section 3.4, we examine the impact of the variation of the torus parameters on the intrinsic optical-UV SED in our fitting procedure to make sure the best-fit torus model results in a reasonable accretion disk SED. Our SED fitting indicate that classification of 3C 14 as a red quasar is related to the inclination angle rather than a dustier torus. Using the length of the radio jets as a proxy of AGN maturity (e.g., Podigachoski et al. 2015) indicates that 3C 14 is a mature quasar. Therefore it is unlikely for this source to be in an evolutionary phase in which turns from an obscured quasar into an unobscured one.

The X-ray spectrum is well fit by the accretion disk model implying no significant contribution from a non-thermal component.

–**3C 43** is a CSS quasar with a jet of < 49 kpc and a core contribution of $< 6\%$ at 5 GHz (Akujor et al. 1991; Ludke et al. 1998). The radio emission is best described with a single power-law with an exponential cutoff at FIR wavelengths. Akujor et al. (1991) indicate that this source has a misaligned and asymmetric structure with a sharp bent jet suggesting that the presence of the bent structure in this source could be due to the interaction of the jet with the ISM.

The best-fit torus model is a combination of clumps with a small volume filling factor and a homogeneous disk with low opacity that result in a small amount of obscuration of the optical-UV emission.

As illustrated in Figure 3 the submm data is dominated by non-thermal radiation from the radio structures. The

Table 6
The parameters of the best-fit torus and accretion disk model

Name	R_{in}^1 (pc)	V_C^2 (%)	τ_C^3	τ_D^4	θ_T^5 (°)	θ_{AD}^6 (°)	$M_{BH}/M_\odot (\times 10^9)$	$\log(\lambda_{Edd})^7$	Spin ⁸
3C 009	3.74	1.5	0	1000	52	48±3.5	3.8±1.75	-0.4±0.2	0.98±0.02
3C 014	4.53	77.7	0	100	67	57±3.5	9.6±4.5	-0.4±0.2	0.92±0.02
3C 043	1.80	1.5	45	100	60	70±3.5	2.1±0.96	-1.0±0.2	0.99±0.02
3C 181	2.85	1.5	45	300	52	59±3.5	1.7±0.78	-0.6±0.2	0.92±0.02
3C 186	2.75	1.5	4.5	300	52	62±3.5	1.5±0.69	-0.6±0.2	0.99±0.02
3C 190	5.95	1.5	45	300	60	63±3.5	6.0±2.8	-1.0±0.2	0.99±0.02
3C 191	6.53	1.5	45	300	43	43±3.5	1.8±0.82	-0.6±0.2	0.92±0.02
3C 204	2.59	77.7	0	300	52	55±3.5	2.9±1.33	-1.0±0.2	0.98±0.02
3C 205	5.79	7.7	4.5	300	52	55±3.5	9.8±4.5	-0.8±0.2	0.92±0.02
3C 208	2.09	1.5	4.5	300	52	48±3.5	1.5±0.69	-0.4±0.2	0.99±0.02
3C 212	1.71	7.7	4.5	300	60	53±3.5	6.0±2.8	-1.20±0.2	0.96±0.02
3C 245	7.94	1.5	0	30	19	26±3.5	1.1±0.51	-0.6±0.2	0.98±0.02
3C 268.4	2.29	1.5	45	1000	52	52±3.5	6.2±2.9	-1.0±0.2	0.99±0.02
3C 270.1	2.55	1.5	45	1000	52	50±3.5	4.6±2.1	-1.0±0.2	0.98±0.02
3C 287	1.16	38.5	0	1000	19	26±3.5	1.5±0.69	-1.2±0.2	0.99±0.02
3C 318	1.30	1.5	45	1000	33	38±3.5	2.4±1.1	-1.6±0.2	0.98±0.02
3C 325	0.75	1.5	13.5	300	60	49±3.5	3.8±1.75	-1.4±0.2	0.88±0.02
4C 16.49	1.19	7.7	0	1000	43	55±3.5	2.1±0.97	-1.4±0.2	0.94±0.02
3C 432	3.07	38.5	0	1000	33	46±3.5	4.7±2.2	-1.2±0.2	0.99±0.02
3C 454.0	4.53	1.5	4.5	1000	43	51±3.5	0.83±0.38	0.00±0.2	0.99±0.02

- 1) The inner radius of the best-fit torus ($R_{in} = r_{in} \times \sqrt{L_{AGN}/10^{41}}$)
- 2) The clumps volume filling factor
- 3) The optical depth of the individual clumps
- 4) The optical depth of the homogeneous disk midplane
- 5) The inclination angle from the best-fit torus model (in degrees)
- 6) The inclination angle from the best-fit accretion disk (in degrees)
- 7) The Eddington ratio, λ_{Edd} which is L_{bol}/L_{Edd}
- 8) The dimensionless spin parameter $a \equiv Jc/GM_{BH}^2$ where J is the angular momentum of the BH

Table 7
The parameters of the best-fit radio model

ID	Best radio model	ν_t	$\nu_{t,jet}$	α_1	α_2	β	ν_{cutoff}	$\nu_{cutoff,jet}$
3C 009	model2	5.5e+07	-	-0.09	-1.04	-	5.7e+11	-
3C 014	model2	3.8e+10	-	-0.91	-2.15	-	1.0e+13	-
3C 043	model1	-	-	-	-0.75	-	1.5e+12	-
3C 181	model1	-	-	-	-0.94	-	8.1e+11	-
3C 186	model3	5562.3	-	-	-	10.28	8.3e+12	-
3C 190	model2	4.7e+07	-	1.98	-0.92	-	4.9e+12	-
3C 191	model1	-	-	-	-0.99	-	3.0e+12	-
3C 204	model2	1.1e+07	-	1.37	-1.10	-	1.0e+12	-
3C 205	model2	5.1e+07	-	1.34	-0.98	-	2.1e+11	-
3C 208	model2	1.9e+08	-	-0.14	-1.16	-	1.0e+12	-
3C 212	model4	1000.1	1.5e+10	2.20	-0.52	7.46	5.0e+11	7.5e+11
3C 245	model4	3814.4	7.9e+08	2.50	-0.35	9.41	8.1e+12	5.0e+11
3C 268.4	model2	6.9e+09	-	-0.71	-1.17	-	3.0e+12	-
3C 270.1	model2	5.6e+07	-	1.35	-0.90	-	1.0e+12	-
3C 287	model2	1.8e+09	-	-0.13	-0.79	-	1.3e+12	-
3C 318	model2	4.3e+08	-	-0.07	-1.01	-	2.0e+11	-
3C 325	model2	1.7e+09	-	-0.50	-1.12	-	2.2e+11	-
4C 16.49	model2	4.2e+08	-	-0.40	-1.17	-	1.0e+11	-
3C 432	model2	1.1e+09	-	-0.64	-1.19	-	2.8e+11	-
3C 454.0	model3	600.4	-	-	-	5.92	1.8e+12	-

best-fitted accretion disk template also confirms the presence of significant non-thermal X-ray component.

–**3C 181** has a radio jet of 65 kpc with <1% core contribution at 5 GHz (Mantovani et al. 1992). The radio emission is best described with a single power-law with an exponential cutoff at 814 GHz. Willott et al. (2002) investigate the 850 μ m band Scuba observation of this source and predict no non-thermal component contributing to this wavelength.

The best-fit torus is a combination of clumps with a small filling factor and a homogeneous disk with moderate opacity which results in little correction of the optical-UV emission.

Comparing the best-fit accretion disk with the X-ray data does not indicate the presence of an underlying non-

thermal X-ray component.

–**3C 186** is a very well studied CSS (O’Dea 1998) with radio jets of 20 kpc and 4% core contribution at 5 GHz (Spencer et al. 1991; Ludke et al. 1998). The radio emission is best described with a parabola (a combination of multiple power-laws). MERLIN observation at 1.6 MHz indicates a one-sided jet and two bent lobes at 60° and 90° with respect to the source axis, creating a S-shaped source (Spencer et al. 1991; Ludke et al. 1998). The curvature in the lobes is presumably due to the sufficiently dense ISM that affect the expansion of the radio structure.

The best-fit torus is a combination of clumps with a small filling factor and a homogeneous disk with moderate opacity which results in no significant correction of

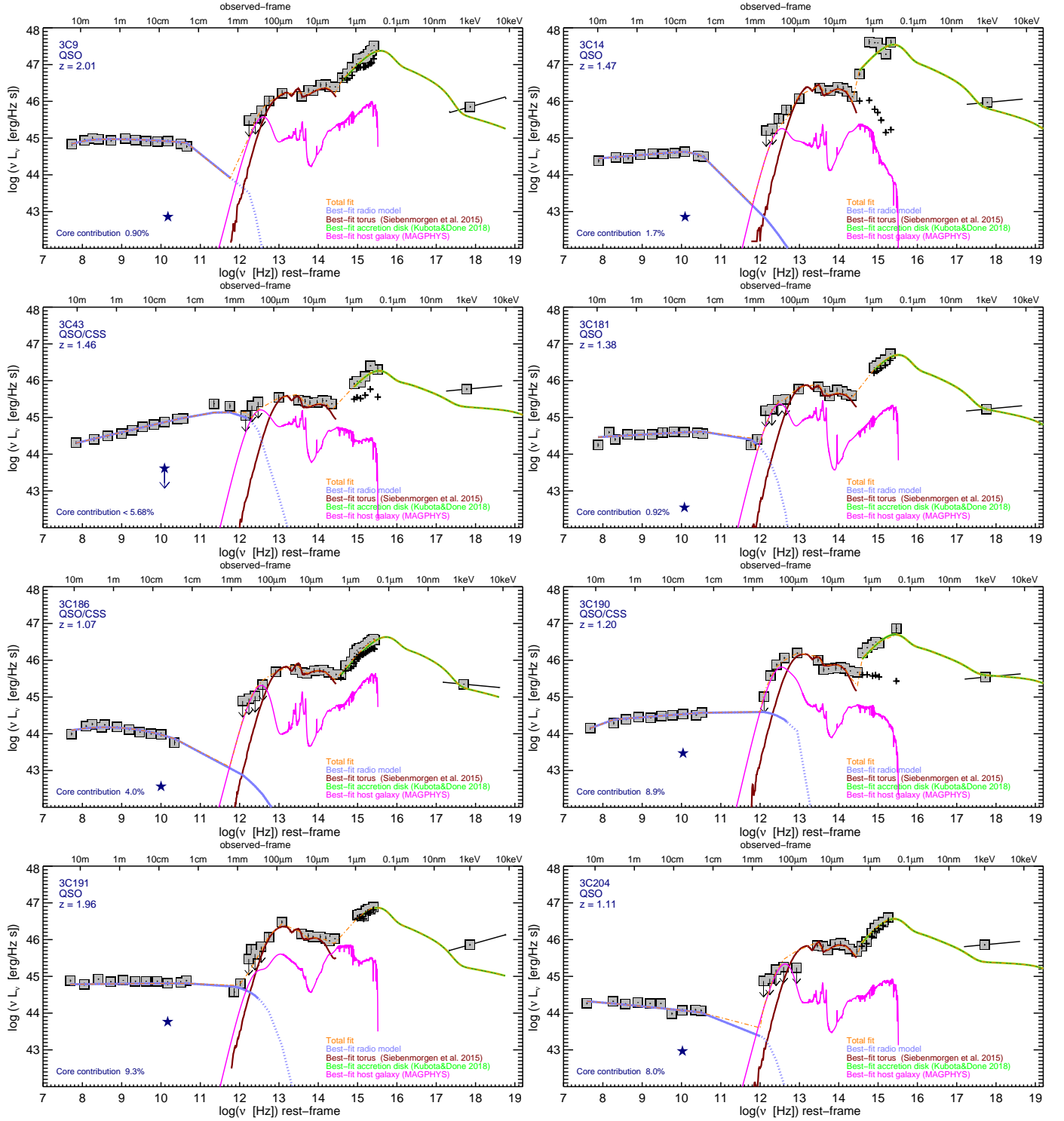


Figure 3. The full suite of photometry with the best-fit models. The gray data points are the absorption corrected broadband photometry, and the black plus signs in optical-UV bands are the photometric points before the torus obscuration correction. The components are: radio component from the core, jets and lobes (light blue), infrared emission from the torus (dark red), the accretion disk component that accounts for the thermal optical to X-ray emission (green), the host galaxy component obtained from MAGPHYS SED fitting code (magenta) and the total fit (orange). The dark blue star indicates the core contribution to the 5 GHz photometry estimated from the R_{CD} .

the optical-UV emission.

The *Chandra* and *Hubble Space Telescope* (*HST*) observations indicate that 3C 186 lives in an over-dense region which is most likely a cluster of galax-

ies (Hilbert et al. 2016; Siemiginowska et al. 2010). The *HST* images indicate a blob of star formation activity 2'' (corresponding to ~ 16 kpc at $z \sim 1$) away from the central engine, perpendicular to the direction of the jets (see

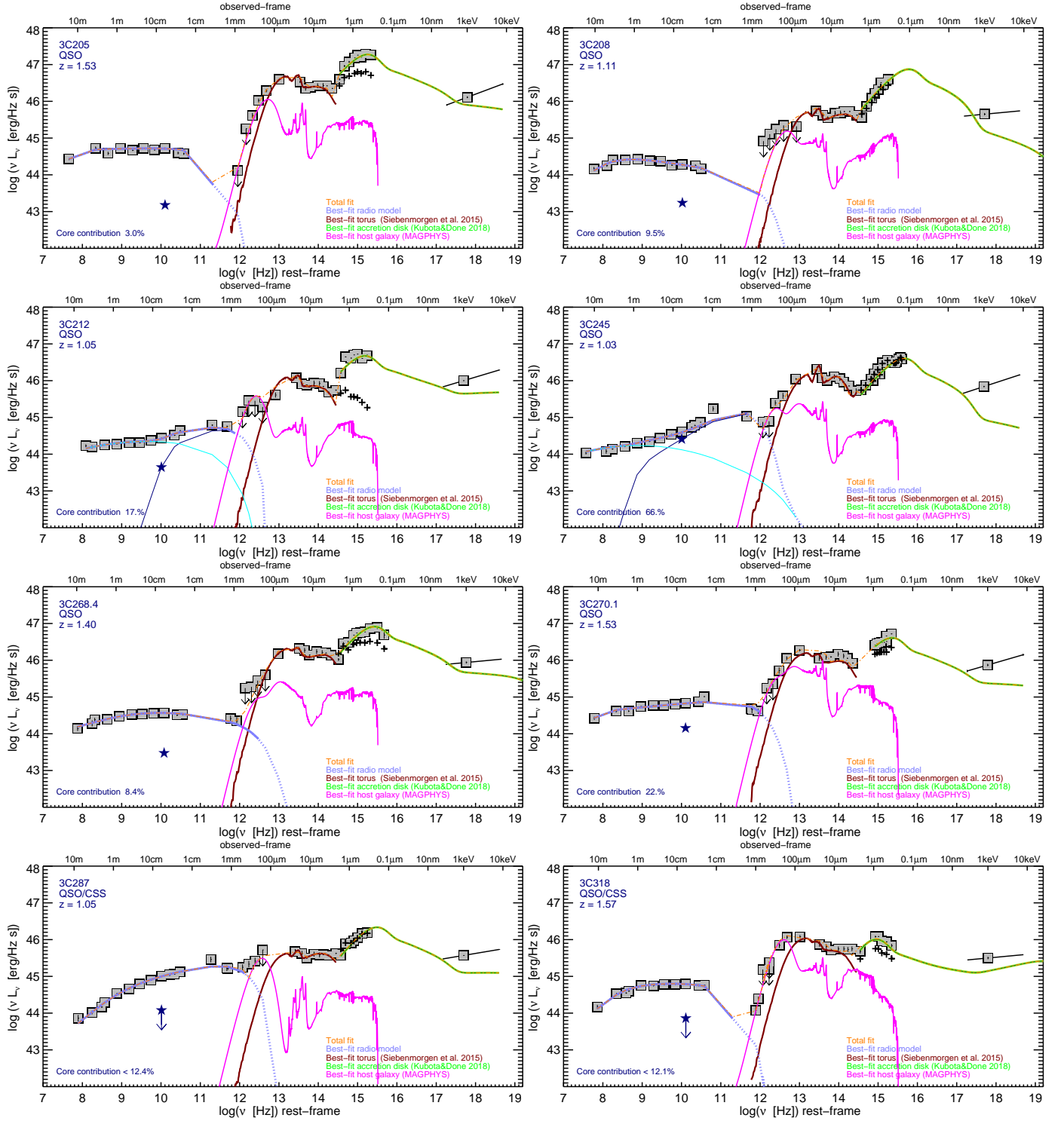


Figure 3 (Cont.).

Figure 10 in Hilbert et al. 2016). This blob could be either from the star formation activity of other members of the cluster or from the host galaxy itself. In latter case, given that the jets' direction is perpendicular to the blob, the star formation activity is not jet-related. Comparing the best-fit accretion disk with the X-ray data does not indicate the presence of an underlying non-thermal X-ray component.

–**3C 190** is a red quasar (Ishwara-Chandra et al. 2003) CSS and has a de-projected radio jet length of 124 kpc, and less than 1% core contribution at 5 GHz. The radio images (Spencer et al. 1991; Ludke et al. 1998) indicate multiple features that require a double-power law in our fitting procedure (see Table 7). As shown in Figure 3, the radio emission cutoff occurs at FIR wavelengths. While this suggests that the non-thermal emis-

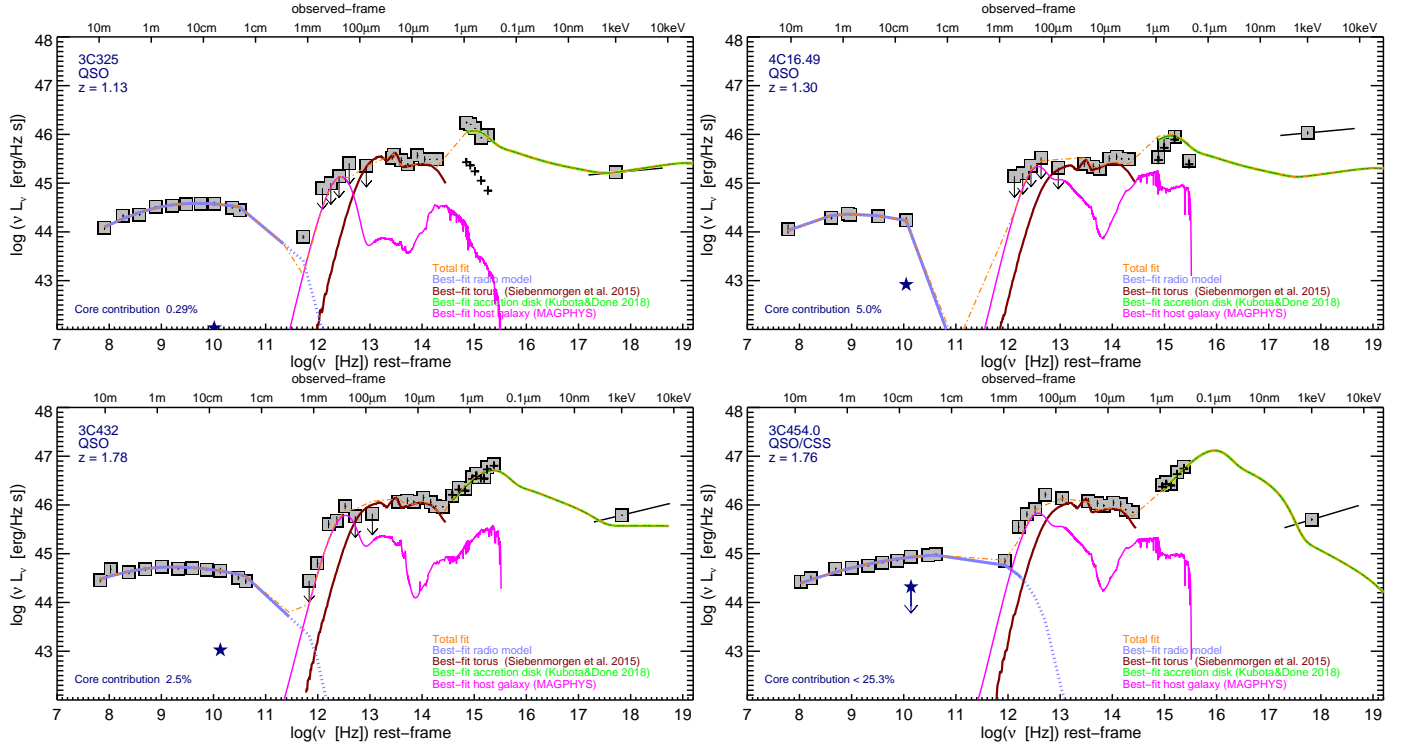


Figure 3 (Cont.).

sion may contribute significantly to the submm wavelengths (hence SFR estimates based on submm data should be treated carefully), submm observations are required for constraining the radio fit.

The emission from the torus is best described with a combination of clumps and a homogeneous disk with maximum acceptable opacity in the torus library (see Table 4). This combination with a small filling factor and 43° inclination angle result in moderate obscuration of the optical-UV emission of the accretion disk. While quasars spectra, in general, show silicate emission feature, the rest-frame $9\text{--}16\ \mu\text{m}$, spectra of 3C 190 indicate the presence of silicate absorption (Leipski et al. 2010). In our fitting procedure, we examined the torus templates with silicate absorption, however, none of those results in better fit compared to that shown in Figure 3.

Comparing the best-fit accretion disk with the X-ray data does not indicate the presence of an underlying non-thermal X-ray component.

–**3C 191** was classified as a CSS in some earlier studies (Akujor & Garrington 1995; Willott et al. 2002), however, using the classification of Podigachoski et al. (2015) and radio jet of 81 kpc we do not classify this object as a CSS. 3C 191 has $\sim 9\%$ core contribution at the 5 GHz and its radio emission is best described as a single power-law with a cutoff at FIR wavelengths (see Table 7). Therefore, as illustrated in Figure 3 the submm data and likely FIR as well has significant non-thermal contribution.

The emission from the torus is best described with a combination of clumps with low volume filling factor and a homogeneous disk with moderate opacity and a inclination angle of 43° which implies no significant obscuration of the accretion disk emission. The low level of obscuration is consistent with the optical spectral slope, α_{opt} , of 0.7 (Barthel et al. 1990) that is typi-

cal value of radio quasars with little obscuration (see also Brotherton et al. 2001; Willott et al. 2002).

3C 191 spectra indicate the presence of a strong absorbing system ($6.1\ \text{\AA}$) associated with C IV absorption line (Anderson et al. 1987) in the vicinity of the radio hot spots (Hamann et al. 2001). Studies find that quasars with strong associated absorption lines are in the early stage of their development and smaller/younger radio structures are more common to have associated absorption lines (e.g., Becker et al. 2000, 2001; Willott et al. 2002). Presence of these absorbing systems distant from the quasar’s core may be associated with a blowout from nuclear starburst (Hamann et al. 2001).

In most of our sources (see Figure 3) the torus component dominates the blue side of the FIR bands; interestingly in 3C 191, it dominates over the host galaxy emission at all the MIR-FIR bands. The Herschel upper limits in the FIR allow for the possibility of a weak, FIR, cool dust contribution below the submm waveband where the synchrotron component dominates. We note that 3C 191 is classified as a hyperluminous quasar with $L_{\text{FIR}} > 1.2 \times 10^{13} L_\odot$ in which quasar heated dust is the dominant source of IR radiation (Willott et al. 2002).

Finally, we note that the best-fitted accretion disk model indicates the presence of a non-thermal X-ray component.

–**3C 204** has an extended jet of ~ 543 kpc and $\sim 8\%$ core contribution in the 5 GHz band. The quasar radio SED is well fitted with a broken power-law (see Table 7). The VLA 4.9 GHz images show multiple features including a bright radio core, hot spots, and a one-sided jet that deflects towards the end (Bridle et al. 1994). There is some evidence of [O II] emission perpendicular to the jet axis (Bremer et al. 1992; Bridle et al. 1994) at ~ 90 kpc towards the north and ~ 45 kpc towards the south.

The emission from the torus is best described with a combination of clouds with negligible optical depth and a homogeneous disk with moderate opacity. This combination with a inclination angle of 52° results in no significant obscuration of accretion disk at optical-UV.

Comparing the best-fitted accretion disk model with the X-ray data suggests the presence of additional, non-thermal X-ray emission.

–**3C 205** has an extended radio structure of ~ 251 kpc with a core contribution of 3% in the 5GHz band. The radio emission is best described as a broken power-law (see Table 7) which is consistent with the presence of the multiple radio structures (Lonsdale & Barthel 1984, 1986).

The emission from the torus is best described with a combination of clumps with small opacity and a homogeneous disk with moderate opacity which result in small amount of obscuration of the accretion disk radiation. 3C 205 spectra indicate the presence of a strong absorbing system (3.21 \AA) associated with C IV absorption line (Anderson et al. 1987).

The best-fitted accretion disk model predicts the presence of little non-thermal radiation at X-ray band.

–**3C 208** has an extended radio jet of ~ 172 kpc with $\sim 10\%$ core contribution at 5 GHz. The radio emission is best fitted with a broken power-law that is consistent with the presence of multiple radio features including a bright core and the hot spots (Bridle et al. 1994). 3C 208 has a one-sided jet that is straight for most of its length but deflects towards the end (Bridle et al. 1994).

The emission from the torus is best described with a combination of clumps with a small optical depth and homogeneous disk with moderate opacity which result in no significant obscuration at optical-UV wavelengths. The available *HST* images (F606W and F140W bands) do not indicate any evidence of nearby merging sources (Hilbert et al. 2016).

The X-ray spectrum fitted by the accretion disk model implies some contribution from a non-thermal component.

–**3C 212** is a red quasar (Aldcroft et al. 2003) with a radio jet of ~ 216 kpc and $\sim 17\%$ core contribution at 5 GHz. MERLIN observations at 6 cm and 15 cm (Akujor et al. 1991) indicate multiple features including a bright core that best fitted with the fourth model in our fitting procedure (see Section 3.1.3 and Table 7). To constrain the radio fit we used recent ALMA observations (see Table 2) which is dominated by the non-thermal radiation from the radio structure (Figure 3).

Consistent with its classification as a red quasar our torus model indicates a combination of clumps and a homogeneous disk with moderate optical depth. These components result in moderate obscuration of the accretion disk emission. This target also has X-ray and UV absorbers (Aldcroft et al. 2003).

The X-ray spectrum fitted by the accretion disk model implies the presence of a non-thermal X-ray component.

–**3C 245** is a moderately beamed quasar (with a jet oriented at $< 20^\circ$ to the line of sight, Foley & Barthel 1990; Marin & Antonucci 2016) with a ~ 1067 kpc jet and $\sim 66\%$ core contribution at 5 GHz which is significantly higher than other sources in our sample (see Table 5). The radio emission is best described as a parabola

with an additional core component (the fourth model in Section 3.1.3). To constrain the radio contribution to the FIR we recently obtained the SMA data (see Table 2), which is dominated by the non-thermal radiation from the radio structure (Figure 3). The extreme variability expected in blazars may not be seen in 3C 245 since our recent SMA observation is consistent with older radio data (Geldzahler & Witzel 1981).

Consistent with its classification, the best-fitted torus indicates a combination of clumps with negligible opacity and a homogeneous disk with small opacity. This combination results in no significant obscuration from the clouds and the homogeneous dusty disk. The torus inclination angle (19° , see Table 6) and the accretion disk inclination angle (26°) are consistent with the radio-determined inclination angle (Foley & Barthel 1990; Marin & Antonucci 2016).

The best-fitted accretion disk model also indicates the presence of significant non-thermal X-ray emission. We note that since 3C 245 has nearly a face-on inclination angle and significant underlying non-thermal radiation at radio/submm and X-ray wavelengths, the non-thermal continuum may contribute significantly in the IR-optical-UV bands as well. Given the significant non-thermal emission and quasar’s dominance at optical-UV bands it is unlikely to have a reliable estimate of the host galaxy properties from our SED fits.

–**3C 268.4** has a jet of 205 kpc and $\sim 8\%$ core contribution at 5 GHzs. The radio images (Lonsdale & Barthel 1986; Liu et al. 1992) indicate multiple features including a bright core and double hot spots. The radio emission is best fitted with a double power-law model with a cutoff at FIR wavelengths (see Table 7) resulting in significant non-thermal contribution at submm wavelengths (Willott et al. 2002).

The emission from the torus is best described with a combination of clumps and a homogeneous disk with the highest acceptable opacity in the torus library (see Table 4). However, this combination with a small filling factor and inclination angle of 52° result in small obscuration of the accretion disk emission. Similar to 3C 191, 3C 268.4 is also classified as a hyperluminous quasar with $L_{\text{FIR}} > 2 \times 10^{13} L_\odot$ (Willott et al. 2002). Additionally, its spectra show strong C IV associated absorption (Anderson et al. 1987).

3C 268.4 was reported as a lensed quasar with a foreground cluster at $z \sim 0.35$ (Sanitt 1976). Recent *HST* observations indicate the presence of a bright star-forming clump $2.5''$ from the center and an additional oblong source with both optical and radio emission $0.8''$ from the center (see Figure 10 in Hilbert et al. 2016). Since the IR emission from these structures cannot be resolved from AGN emission with the current data, the hyperluminous quasar classification should be treated with caution (see 3C 318 below).

The X-ray spectrum fitted by the accretion disk model implies no significant contribution from a non-thermal component.

–**3C 270.1** has a jet of ~ 374 kpc and a relatively high core contribution (22%) at 5 GHz. Multi-frequency radio images of 3C 270.1 indicate the presence of strong core and hot spots (Liu et al. 1992) and a one-sided jet (Hilbert et al. 2016). The radio emission is best fitted with a double power-law with a cutoff at FIR wave-

lengths resulting in significant non-thermal contribution at submm wavelengths.

The emission from the torus is best described with a combination of clumps with a small filling factor and a homogeneous disk with the highest acceptable opacity in the torus library. This combination with a 52° results in little reddening of the accretion disk emission.

3C 270.1 spectra indicate the presence of a strong absorption complex ($> 6.17 \text{ \AA}$) associated with C IV absorption line (Anderson et al. 1987).

The best-fitted accretion disk model indicates the presence of significant non-thermal emission at X-ray waveband. *Chandra* observations find extended X-ray emission that is co-spatial with the radio lobe and peaks at the position of the hot spots (Wilkes 2011). The extended X-ray emission is not included in the X-ray data used for this SED analysis.

–**3C 287** is a CSS with a projected radio jet of ~ 8 kpc. Because the jet inclination angle for this object is unknown, we were unable to estimate its de-projected jet length. Also we were unable to find the R_{CD} value for this object, therefore adopted the average value of the CSS quasars in our sample (Section 3.1.3) which resulted in $\sim 10\%$ core contribution. The radio emission is modeled as a double power-law with a cutoff at submm/FIR wavelengths (see Table 7,) resulting in significant non-thermal contribution at submm wavelengths. The VLBI and MERLIN observations indicates the presence of multiple radio structures including a curving jet (Fanti et al. 1989).

The emission from the torus is best described with a combination of clumps with a negligible optical depth and a homogeneous disk with the highest acceptable opacity in the torus library (see Table 4). This combination with the inclination angle of 19° (26° from the accretion disk model) result in no significant obscuration of the optical-UV radiation from the accretion disk. While the extreme variability is expected in moderately beamed quasars, it may not be seen in CSS and GPS sources such as 3C 287 since they are young (e.g., Conway 2002; Salvesen et al. 2009).

The X-ray spectrum fitted by the accretion disk model implies a significant contribution from a non-thermal component. The X-ray data obtained with XMM-Newton and *Chandra* (Salvesen et al. 2009; Wilkes et al. 2013) find a soft X-ray spectrum ($\Gamma=1.8$) that can be fitted with a simple power-law.

Similar to 3C 245, 3C 278 is viewed almost face-on and has significant underlying non-thermal radiation at radio/submm and X-ray wavelengths. The non-thermal continuum may contribute at other wavelengths. We also note that the *HST* images indicate a few nearby sources ($\sim 5''$, Hilbert et al. 2016) and the IR emission may be contaminated by one/more of these sources. All together, these make the host galaxy properties estimated from our SED fits uncertain.

–**3C 318** is a CSS with a jet of ~ 8 kpc and core contribution $< 12\%$ at 5 GHz. The 18 cm MERLIN and VLBI observations (Spencer et al. 1991) show a two-sided jet which fades before reaching the lobes. The emission from the radio structure is best described with a double power-law with a cutoff at 200 GHz. In addition to the 1.2 mm MOMBO data we used recent ALMA observations (see

Table 2 and Barthel & Versteeg 2019) to constrain the radio model. Barthel & Versteeg (2019) used the 2 cm VLA image to subtract the non-thermal emission from the ALMA image at 1mm and estimated that $\sim 11\%$ of the total flux at 1 mm has a non-thermal origin. We use this estimate to constrain the radio model in our fitting procedure. However, with this prior estimate, the cutoff in our fitting procedure happens at ~ 200 GHz consequently, we estimate no non-thermal contribution at 1 mm. Therefore there could be $\lesssim 10\%$ non-thermal contribution at submm wavelengths.

The torus emission is best described with a combination of clumps and a homogeneous disk both with high opacity. However, due to the small filling factor of the clumps and the 33° inclination angle these components do not result in a significant obscuration of the accretion disk emission.

The best-fit accretion disk indicates presence of non-thermal X-ray emission. We note that with only few data points at optical, UV, and X-ray range the physical parameters driven from the accretion disk model (see Table 6) should be treated with caution.

We note that 3C 318 is classified as a hyperluminous infrared quasar with $L_{FIR} > 10^{13} L_\odot$ in some earlier studies (Willott et al. 2002, 2007). Recently, Podigachoski et al. (2016b) reported that most of the fluxes measured in earlier studies originate in a pair of bright interacting galaxies at $z \sim 0.35$. To robustly estimate the AGN and host galaxy properties, we used the fluxes from Table 1 in Podigachoski et al. (2016b). After subtracting the contamination of the nearby source from the photometry, 3C 318 has an SFR of $\sim 320 M_\odot/\text{yr}$ factor of 5 lower than the Willott et al. (2007) estimation.

–**3C 325** was originally classified as a radio galaxy, and later was reclassified as a red quasar (Grimes et al. 2005) based on optical spectroscopic data. This quasar has a projected radio jet of 124 kpc and less than 1% core contribution at 5 GHz. Because the jet inclination angle for this object is unknown, we were unable to estimate its de-projected jet length. The VLA images show multiple features including bright hot spots and asymmetrically placed lobes (Fernini et al. 1997). The radio data is best fitted with a double power-law which turns down before reaching the submm wavelengths.

Consistent with its classification the emission from the torus is best described with a combination of clumps and a homogeneous disk with moderate opacity. This combination results in moderate obscuration of the accretion disk emission. Considering the lack of data in $1\text{--}3 \mu\text{m}$ (observed-frame) the best-fit accretion disk is determined with the data points at shorter wavelengths, therefore the accretion disk parameters are not well constrained.

The best-fit accretion disk does not imply presence of non-thermal X-ray emission. The X-ray analysis indicates a moderately hard X-ray spectrum with the hardness ratio, $(H-S)/(H+S)$, where H and S are the net count rates in the 2–8 keV and 0.5–2 keV X-ray bands) of +0.05 which is harder than all the other quasars in our sample (Wilkes et al. 2013).

–**4C 16.49** has a radio jet of 216 kpc with a 5% core contribution at 5 GHz. The radio images obtained with VLA at 2 and 6 cm show a strong radio core, jet and a small counter jet (Lonsdale et al. 1993). The radio emis-

sion is best described with a double power-law (see Table 7). Due to the small number of reliable data points and lack of submm data we should be cautious in interpreting the optimization results and interpretation of the non-thermal contribution from the radio structure at shorter wavelengths.

The best-fit torus model is a combination of clumps with negligible opacity and a homogeneous disk with the highest acceptable opacity in the torus library (see Table 4). This combination results in no significant obscuration of optical-UV emission from the accretion disk.

The best-fitted accretion disk template also confirms the presence of significant non-thermal X-ray component. However, unlike other sources in our sample, 4C 16.49 do not have SDSS or other recent reliable data at optical-UV wavelengths and is only limited to old SuperCOSMOS observations. Given the limited number of optical-UV photometric measurements, the accretion disk may not be well-constrained and the modeled non-thermal X-ray component may not be significant.

– **3C 432** has jet of ~ 155 kpc and core contribution of $\sim 3\%$ at 5 GHz. The VLA images indicate multiple structures including radio lobes, bright hot spots, and a one-sided jet (Bridle et al. 1994). The emission from these radio structures is best described with a double power-law (Table 7).

The torus emission is best fitted with a combination of clumps with negligible opacity, and a homogeneous disk with high opacity that are viewed at 33° and result in no significant obscuration of the accretion disk emission. The *HST* F606W and F140W images show an extended narrow line regions (within $8''$) along the direction of the radio lobes (Hilbert et al. 2016) with several faint sources within this radius which could potentially contaminate the quasar SED.

The X-ray spectrum fitted by the accretion disk implies no contribution from a non-thermal component to the X-ray emission.

– **3C 454.0** is a CSS with a de-projected jet of < 46 kpc and $< 25\%$ core contribution at 5 GHz. The radio images show various features, including the core and hot spots (Spencer et al. 1991; Ludke et al. 1998). The radio emission is best described with a parabola having a cutoff at FIR wavelengths. To constrain the radio model we added recent ALMA data to our analysis (see Table 2 and Barthel & Versteeg 2019). We used the non-thermal emission estimated in Barthel & Versteeg (2019) as prior information to constrain the radio model in our fitting procedure. Similar to Barthel & Versteeg (2019) we estimate $\sim 82\%$ non-thermal emission at 1mm.

The torus emission is best fitted with a combination of clumps with small opacity, and a homogeneous disk with the maximum acceptable value in the torus library (see Table 4). This combination at inclination angle of 43° result in no significant obscuration of the accretion disk emission.

The X-ray spectrum fitted by the accretion disk implies contribution from a non-thermal component at X-ray wavelengths.

4.2. Commonalities Among Sources

– Out of the 20 quasars in our sample, ten (3C 43, 3C 181, 3C 190, 3C 191, 3C 212, 3C 245, 3C 268.4, 3C 270.1, 3C 287 and 3C 454.0) have significant non-thermal con-

tamination ($> 70\%$) at 1 mm. To robustly estimate the SFR based on submm observations it is important to subtract any source of contamination from the broad-band photometry.

– In 13 sources (3C 9, 3C 43, 3C 191, 3C 204, 3C 208, 3C 212, 3C 245, 3C 268.4, 3C 270.1, 3C 287, 3C 318, 4C 16.49 and 3C 454.0) the best-fit accretion disk confirms the presence of a significant non-thermal X-ray component.

– In sources with small inclination angles (3C 245 and 3C 287) the significant underlying non-thermal radiation at radio/submm and X-ray wavelengths, may contribute at IR-optical-UV bands as well. Therefore, the torus and the host galaxy properties derived from SED fitting are likely to be uncertain.

– The *HST* (F606W and F140W bands, Hilbert et al. 2016) of some of our sources (3C 268.4, 3C 287 and may be 3C 432) indicate the presence of a few nearby objects which may contaminate the photometry. In these cases the host galaxy properties estimated from SED fitting may be overestimated.

– Four quasars in our sample, 3C 191, 3C 205, 3C 268.4, 3C 270.1, with de-projected radio jets of 81, 251, 205 and 374 kpc have associated C IV absorption complexes (Anderson et al. 1987) with equivalent width of 6.12 \AA , 3.21 \AA , $> 1.87 \text{ \AA}$ and $> 6.17 \text{ \AA}$, respectively. While some studies (e.g., Becker et al. 2000, 2001; Willott et al. 2002) suggest that associated absorption is more common in sources with smaller/younger radio structures, there does not appear to be such a relationship in our sample.

– Our SED modeling is limited by the number of reliable photometry (see Section 5.1). In sources with few reliable optical-UV data points (3C 14, 3C 318, 3C 325 and 4C 16.49) the accretion disk parameters may not be well constrained.

5. RESULTS AND DISCUSSION

In this study we present a state-of-the-art AGN radio-to-X-ray SED model (ARXSED) that decomposes radio-loud quasars into their AGN and host galaxy components by fitting their photometry over ten decades in frequency space. With ARXSED we investigate the properties of a sample of 20 3CRR quasars at $1 < z \lesssim 2$. Below we first discuss the uniqueness and limitations of our technique, as well as the average properties of the AGN in our sample. We then present the median SED of the radio-loud quasars obtained with our fitting technique. Finally, we compare the details of our model, the median SED, and properties of our quasars with the literature.

5.1. Uniqueness, Limitations and Biases of ARXSED

An advantage of this study compared to previous work (e.g., Kuraszkiewicz et al. 2003; Mullaney et al. 2011; Podgachoski et al. 2015, 2016b) is the wavelength coverage. ARXSED treats photometry extending from radio to X-ray wavelengths. Specifically, ARXSED models the radio emission (Section 3.1.3), the torus (Section 3.1.2) and the accretion disk (Section 3.1.1) as well as the host galaxy (Section 3.2). Thus it simultaneously accounts for radiation from different structures surrounding the SMBHs. While ARXSED considers a component that account for the host galaxy emission from radio to UV wavelengths, some studies rely on scaling re-

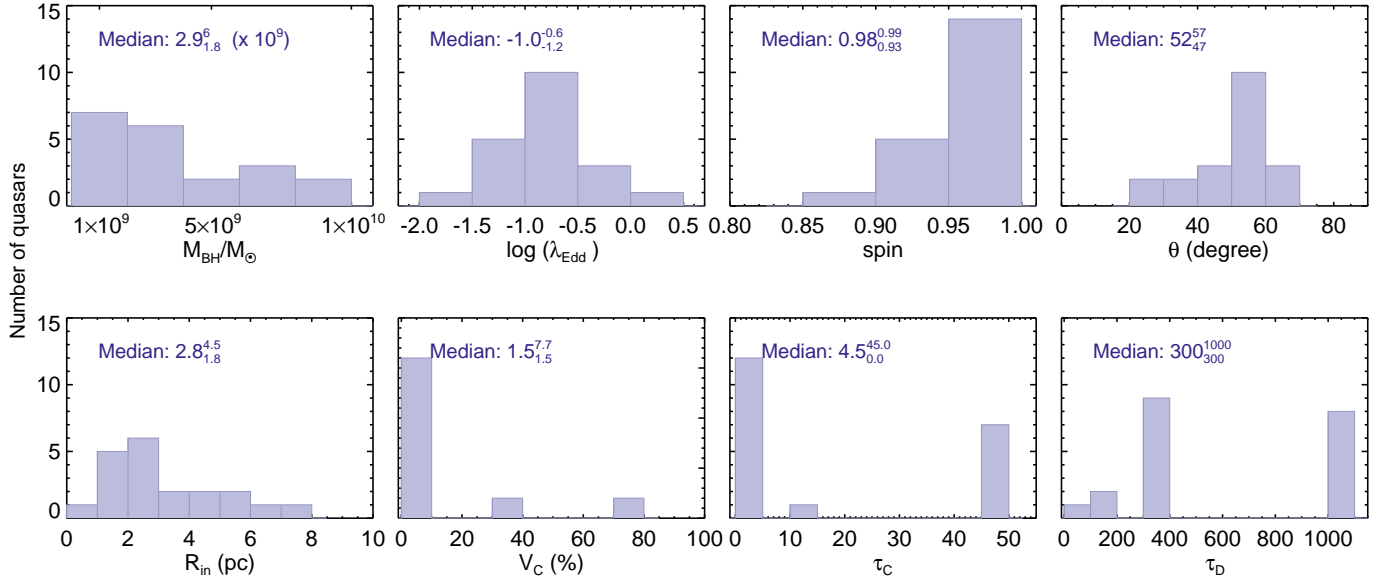


Figure 4. The distribution of the physical properties of the AGN derived from the accretion disk and the torus fits for our 3CRR quasars, along with the median values in each case and their associated 25th-75th percentile ranges.

lations such as $M_{BH} - \sigma$ (e.g., Hunt 2003), $L_{host} - L_{AGN}$ (Vanden Berk et al. 2006) or color-color diagnostics (e.g., Grewing et al. 1968; Sandage 1971; Elvis et al. 2012) to account for the host contribution. Considering the uncertainty and large scatter in each of these scaling relations, the physical properties of the AGN derived from their analysis may not be robust.

Like most modern SED fitting codes, ARXSED implements a self-consistent approach to dust attenuation, in which the *intrinsic* SED of radio-loud quasars is appropriately corrected for the reddening and absorption occurring in the torus, the host galaxy, and along the line of sight in the Milky Way.

The main limitations to our approach are from a lack of reliable photometry. Several sources in our sample (e.g., 3C 325, 4C 16.49) lack reliable optical-UV photometry and/or have very few data points, leaving their accretion disk parameters poorly constrained.

ARXSED uses the thermal optical-to-X-ray continuum fitting (Zhang et al. 1997) technique to constrain the SMBH and the accretion disk properties. Constraining the accretion disk parameters without observations around the peak of the thermal continuum is challenging. The peak of the accretion disk is sensitive to the BH mass, Eddington ratio and the spin (see Figure 1), therefore not having good constraints results in larger uncertainties. To accurately determine the peak of this thermal continuum (occurring around 100-1000Å rest-frame for SMBHs) we require far-UV (FUV) observations from space (e.g., the Cosmic Origins Spectrograph on *HST*), and soft X-ray data contributing to the high energy part of the thermal continuum.

Another advantage of ARXSED is that it implements multi-component radio models that account for a steepening or cut-off due to the aging of the electron populations. We find that a single power-law ($L_\nu \propto \nu^\alpha$) can not adequately model the radio emission when compact structures like cores and hot spots are present. In addition, the long-wavelength radio photometry usefully constrains the non-thermal radiation from the radio structures at shorter wavelengths. However, a lack of submm

data and high S/N Herschel observations may result in underestimation of the non-thermal contamination in some cases (e.g., 3C 204), and a corresponding overestimate of SFR.

ARXSED is based on the assumption that the photometry is dominated by the radiation from the AGN at most wavelengths (except for the FIR; see Section 3.4), therefore we may underestimate the stellar mass in some sources. Also in sources with small inclination angles (3C 245 and 3C 287, see Table 6) beamed non-thermal emission at IR-optical-UV wavelengths, unaccounted in our modeling, add uncertainty to the derived host galaxy properties. We will discuss the results and the limitations of our technique for SFR and stellar mass measurements in detail in a following paper (Azadi et al. 2020b, in prep).

5.2. Physical Properties of the SMBHs and Dusty Tori in 3CRR Quasars

The distributions of the SMBH, torus and accretion disk properties derived from the SED fits for our 3CRR quasars are shown in Figure 4, along with the median values in each case. The M_{BH} , $\log(\lambda_{Edd})$ and spin are constrained by the best fit accretion disk (see Table 6). The inner radius of the torus, the volume filling factor, optical depths of the dust clouds, and the homogeneous dusty disk are constrained by the torus model. The inclination angle (measured from the pole) is the average value driven from the best fit torus and the accretion disk.

The average BH mass of the quasars in our sample is $3.7e+9 \pm 2.7e+9$ (standard deviation) M_\odot . While the BH masses in our analysis are obtained from the best-fit accretion disk templates, the templates are built based on initial mass estimated from either C IV $\lambda 1548$ or Mg II $\lambda 2800$ emission lines (Section 3.1.1). We used this mass as an initial estimate for building the QSOSED templates and the $\log(M_{BH})$ is allowed to vary within ± 1 dex of this initial estimate (see Table 3). Using C IV $\lambda 1548$, Mg II $\lambda 2800$ or H β $\lambda 4863$, McLure et al. (2006) estimated M_{BH} for 18 out of 20 quasars in our

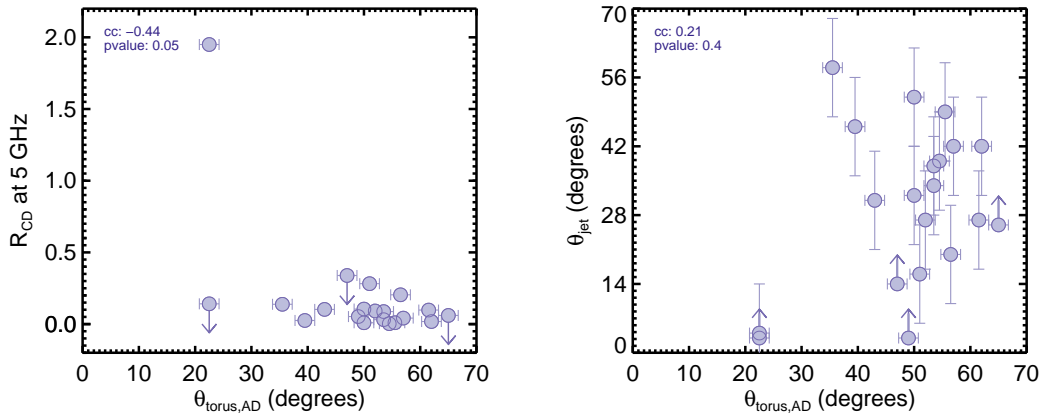


Figure 5. *Left:* The relation between the radio core dominance R_{CD} and the average inclination angle of the torus and accretion disk. Quasars with smaller torus/accretion disk inclination angles have higher core fractions. *Right:* The relation between the jet inclination angle and the average inclination angle of the torus and accretion disk. There is no significant correlation between the two angles.

sample (except for 3C 318 and 3C 325) and obtained an average of $3.8 \pm 2.9 \times 10^9 M_{\odot}$. Indeed our estimates of the 3CRR BH masses are consistent with the BH mass estimates of the non-3C radio-loud AGN at similar redshifts (e.g. Liu et al. 2006). Recently, Collinson et al. (2015, 2017) investigated the intrinsic NIR to X-ray SED of 11 radio-quiet quasars at $1.6 < z < 2.2$. Using $H\alpha$ $\lambda 6565$ line they estimate they estimate an average BH mass of $1.5 \pm 1.4 \times 10^9 M_{\odot}$. With a larger sample at $z < 0.5$, McLure & Dunlop (2002) find that radio-loud quasars have larger BH masses than their radio-quiet counterparts although with a large overlap. Laor (2000) also find a distinction between the BH mass of the radio-loud and radio-quiet PG quasars with former having BH mass $> 1 \times 10^9 M_{\odot}$.

The average quasar $\log(\lambda_{Edd})$ is -0.87 ± 0.41 using the QSOSED templates of Kubota & Done (2018). However, lack of the FUV and soft X-ray data can bias the measurements towards more massive black holes and/or lower Eddington ratios (Section 5.1). Adopting the SMBHs masses from McLure et al. (2006), and the bolometric correction from Heckman et al. (2004) for estimating L_{bol} from $L_{[OIII]}$, recently Daly (2019) estimated the average $\log \lambda_{Edd}$ for 15 of the quasars in our sample to be -0.32 ± 0.42 . Given the scatter in the average values and different methodology used in estimating $\log(\lambda_{Edd})$ the differences between their findings and ours are not significant. Adopting the accretion disk model of Done et al. (2012), OPTXAGNF, Collinson et al. (2015) estimate an average of $\log(\lambda_{Edd})$ of 0.02 ± 0.57 which is not significantly different than the average for our sample. Indeed, Figure 1 in Kubota & Done (2018) illustrates the fairly small differences in shape and normalization between the QSOSED and OPTXAGNF models.

Another parameter estimated from our accretion disk modeling (i.e., thermal continuum fitting) is the SMBH spin. The average spin of the quasars estimated from the best-fit accretion disk is 0.97 ± 0.04 . Adopting the OPTXAGNF accretion disk model (Done et al. 2012) Collinson et al. (2017) find their sample quasars have spins < 0.9 . Adopting Blandford & Znajek (1977) framework in which the BH spin is related to the magnetic field, Daly (2019) estimates the spin of 750 SMBHs and for the 15 quasars included in our sample find an average spin of 0.99 ± 0.01 (see also Daly 2011).

We note that although the continuum fitting method can reliably estimate the spin of stellar-mass BHs, its application to AGN can be more challenging. In AGN, the inner accretion disks are relatively cool ($T \sim 10^5$ K) with the bulk of the thermal emission occurring in the far-or-extreme UV regime which is hard to observe from the ground. However, recent studies of SMBHs with well-constrained masses find that spins estimated with the thermal continuum fitting method are in good agreement with estimates from reliable techniques such as the X-ray reflection technique (e.g., Capellupo et al. 2016).

The best-fit torus parameters indicate low obscuration, consistent with nature of the sources (quasars) in our sample. Indeed all the sources with high filling factor in Table 6 have clumps with negligible optical depth. As expected for red quasars (3C 14, 3C 190, 3C 212, 3C 325) the obscuration of the optical-UV emission from the accretion disk is more pronounced (Figure 3). Also, the negligible optical depth of the clumps in 7 out of 20 quasars in our sample (Table 6) indicates that the primary source of torus obscuration is dust in the toroidal disk rather than the clumps. The average inclination angle (measured from the pole) obtained from the best fit torus and accretion disk is $49^\circ \pm 12^\circ$, which is consistent with other studies of non-blazar radio-loud (broad-lined) AGN (e.g., Willott et al. 2000; Arshakian 2005; Marin & Antonucci 2016). Also Figure 4 indicates that we are not fitting sources with inclination angles $< 20^\circ$, as these would be blazars.

5.3. The Orientation of 3CRR Quasars

We investigate the relation of the radio core dominance, R_{CD} (Section 3.1.3), at 5 GHz and the jets' inclination angle with the average inclination angle of the torus and accretion disk obtained from our best fit in Figure 5. In each panel we report the correlation coefficient and its significance level based on **r-correlate**¹¹ routine in IDL.

In the left panel of Figure. 5 a statistically significant correlation is found where quasars with more face-on (smaller) inclination angles have higher core fractions.

¹¹ **r-correlate** computes the Spearman's rank correlation coefficient (cc) and the significance of its deviation from zero (pvalue). A correlation is considered significant if $pvalue < 0.05$. In this case it is unlikely for the correlation to have occurred by accident.

However, 3C 245, the quasar with the highest R_{CD} and core contribution (66%) in our sample plays an important role in deriving this correlation. The trend we find is as expected based on the Unification model in which the flux of the beamed, jet component decreases as the inclination angle increases. We also examined the relation between R_{CD} and all the other torus parameters (e.g., filling factor, optical depth of the clouds or disk) and the accretion disk parameters and did not find any significant correlation. Given the limited range of R_{CD} of the quasars in our sample ($\sim 0 - 0.4$ without 3C 245), in order to see the variation of the radio core dominance and obscuration with the inclination angle we need to include the edge-on sources. This will be addressed in a later paper, in which we will also compare our SED fits with the clear orientation-dependence of the X-ray obscuration in this sample (Wilkes et al. 2013).

The right panel of Figure 5 shows the relationship between the radio jet inclination angle (taken from Marin & Antonucci 2016, see Table 5) and the average torus/accretion disk inclination angle. Our results indicate that the orientation of these structures do not always line up. We speculate that changes in accretion disk/torus orientation coming after jet launching may ruin any alignments between the two. Therefore the difference is expected to be more noticeable with longer/older jets. A more definitive study will be carried out when we include the radio galaxies which have with a wider range of orientation.

5.4. Comparisons with the Literature on the SED Fitting of 3CR Sample at $1 < z \lesssim 2$

The SED decomposition of 3CR radio sources at different redshifts and wavelengths has been the subject of several studies (e.g. Drouart et al. 2014; Westhues et al. 2016; Podigachoski et al. 2015, 2016b). Podigachoski et al. (2015) investigate 1-1000 μm SED of 3CR quasars and radio galaxies at $1 < z \lesssim 2$ (our parent sample) by fitting the AGN and host galaxy components simultaneously. To model the radiation from the torus they use the Hönig & Kishimoto (2010) clumpy torus model with a modified blackbody component to describe the emission from hot dust in the torus. To model the host galaxy component they use a modified blackbody at FIR wavelengths.

We compared the SEDs of all our sources with those from Podigachoski et al. (2015) to identify any discrepancies between the physical parameters obtained from the two fitting procedures. As noted in Section 3.1.2, in the Siebenmorgen et al. (2015) torus model, fluffy dust grains that are larger than the standard ISM are adopted which can survive closer to the BHs, resulting in stronger NIR radiation as well as more pronounced FIR/submm emission. Therefore our torus model accounts for the radiation from the hot dust grains and contributes more FIR emission than the Podigachoski et al. (2015) approach. This is particularly noticeable in 3C 190 resulting in a significantly lower estimated SFR. Also, Podigachoski et al. (2015) consider the host galaxy emission only at FIR wavelengths while our host galaxy model covers UV to radio wavelengths (although it is not the dominant source of radiation in most of these bands). Another difference is the way upper limits are treated in the two models. Podigachoski et al. treat the upper

limits (especially at 70, 160 and 250 μm) as detections and report the SFR estimated from these bands as upper limits while we do treat them as upper limits. Finally, unlike ARXSED, Podigachoski et al. (2015) do not consider non-thermal radiation from the radio structures in the submm/FIR bands. Overall, these differences result in lower SFR estimates from our fitting procedure than from Podigachoski et al. (2015). We discuss the host galaxy properties (e.g., SFR, stellar mass) and the discrepancies with Podigachoski et al. (2015) more fully in a following paper (Azadi et al. 2020b, in prep).

Podigachoski et al. (2016a) improved upon the approach of Podigachoski et al. (2015) by adopting the Siebenmorgen et al. (2015) torus model and the PÉGASE SED model (Fioc & Rocca-Volmerange 2019) for the host galaxies. However, their improved SED model, which like ARXSED treats the submm-to-UV SED of the torus, was only run for 12 of the Podigachoski et al. (2015) sample sources.

5.5. The Median SED of 3CRR Quasars

Figure 6 presents the median AGN SED (left) and the medians for the individual components (right) in our study. The shaded region around each component shows 25th-75th percentile ranges. Since the number of data points between the radio and FIR is very limited in our sources the scatter around the median is significantly larger in these bands. The gray curve (in the left panel) indicates the median SED of the radio-loud quasars in Elvis et al. (1994) normalized at 1.5 μm and the dotted parts indicate regions with few or no data available in Elvis et al. (1994) sample. The dotted-dashed curve (in the right panel) is the median SED of Podigachoski et al. (2015). The median SED of Elvis et al. (1994) is obtained from 18 X-ray bright radio-loud quasars at $z < 0.8$ after subtracting the host galaxy contribution. The median SED of Podigachoski et al. (2015) is obtained from a sample of 25 3CR radio-loud quasars at $1 < z \lesssim 2$ (our parent sample) using the SED components described in Section 5.4.

The median SED of the Elvis et al. (1994) radio-loud quasars covers a similarly broad frequency range and is in agreement with our median SED. However, the differences between the two are more distinct at some specific bands. Although Elvis et al.'s sample has a lower redshift, given the nature of their selection (X-ray bright), they can still be as bright as our quasars at X-ray wavelengths.

The slope of the hard X-ray power-law in Elvis et al. is flatter than for our sample, which could be due the presence of a radio-linked X-ray component. Elvis et al.'s IR observations were limited to *IRAS* wavelengths, while ours extend to longer wavelengths, and reflect greater IR emission. This could be due to the fact that our sample includes the brightest radio galaxies at $1 < z \lesssim 2$, at the peak of the star formation activity in the Universe. This likely results in our sources being more IR-luminous, compared to Elvis et al. (1994). In addition, our sample galaxies, because of their selection at radio wavelengths, is biased towards very powerful radio emitters and can be expected to exhibit a higher median radio SED than Elvis et al. (1994). Overall, considering the differences at radio and optical-UV wavelengths, the Elvis et al. me-

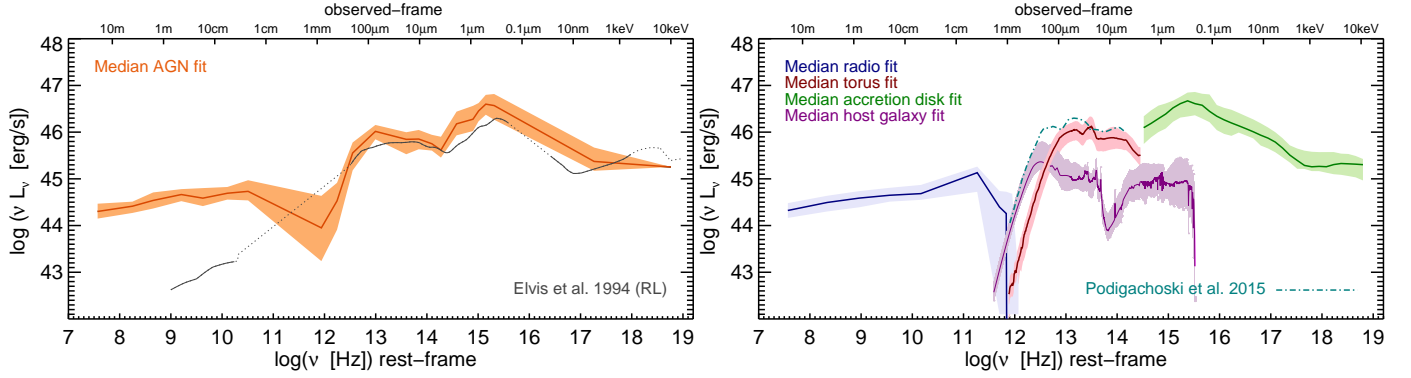


Figure 6. *Left:* The median SED of the total AGN fit in our sample. The gray curve shows the median SED of the radio-loud quasars in Elvis et al. (1994) normalized at $1.5 \mu\text{m}$. The dotted gray curve indicates regions with few or no data available in Elvis et al. (1994) sample. *Right:* The median SED of the each of the components used in this study. The dotted-dashed curve is the median SED of Podigachoski et al. (2015) which is obtained with the AGN and host galaxy components combined. The shaded region around each component indicates the 25th-75th percentile ranges. The small number of photometric measurements between the radio and FIR bands results in a larger scatter around the median in these bands.

dian SED cannot plausibly be said to capture the average behavior of radio-selected AGN at $z > 1$.

Figure 6 also shows the median SED of the quasars (and their host galaxies) from Podigachoski et al. (2015). Given the scatter in the Podigachoski et al. SEDs (0.5-1 dex, not shown for clarity), their median SED is generally consistent with ours. One notable difference is the redder and fainter FIR peak relative to our sample. This could be due to the difference in the torus models i.e., the larger grains adopted in ARXSED, which results in stronger FIR radiation from the torus and consequently less pronounced emission from the host galaxy. We also note that ARXSED subtracts the non-thermal radiation from radio structures in the submm/FIR regime, which can contribute to a fainter FIR peak.

There have been many attempts to describe the average SED of quasars (e.g. Richards et al. 2006). Considering that the Richards et al. (2006) median SED is dominated by radio-quiet AGN (their sample includes only 8 radio-loud sources) it is not shown in Figure 6.

6. SUMMARY

In this study we present a state-of-the-art AGN radio-to-X-ray SED model (ARXSED) that simultaneously fits AGN and the host galaxy components. Using this model we fit the radio-to-X-ray SED of a sample of 20 radio-loud quasars from the 3CRR sample at $1 < z \lesssim 2$. These quasars are low-frequency radio-selected, and so unbiased in terms of orientation and dust obscuration.

In ARXSED, to replicate the emission from the AGN at radio wavelengths, we consider four models. These models account for radiation from the lobes as well as compact radio structures such as radio cores and hot spots where a superposition of various self-absorbed components make the shape of the spectrum more complex. Additionally our model can account for a steepening or cut-off due to the aging of the electron populations. To account for emission from the torus in the infrared we use the two phase torus model of Siebenmorgen et al. (2015) in which the dust can be distributed in a homogeneous disk, or a clumpy medium, or a combination of both. To account for the optical-UV-X-ray radiation from the accretion disk we use the QSSED model developed by Kubota & Done (2018). To account for the emission from the host galaxy we consider an underlying

component from UV to radio wavelengths (MAGPHYS da Cunha et al. 2008, 2015).

We have compiled the radio to X-ray SED of 20 radio-loud quasars from the 3CRR sample at $1 < z \lesssim 2$ by combining archival multi-frequency radio observations, recent SMA/ALMA observations, *Herschel*, *WISE*, *Spitzer*, 2MASS, UKIRT, SDSS, *XMM-Newton* and *Chandra* for our analysis (Section 2). In order to obtain the intrinsic SED of the AGN in our sample, we correct the photometry for the reddening and absorption in the host galaxy, the Milky Way as well as the dusty torus (Section 3.3).

In this paper we present the fitting results for individual sources (Section 4.1) and analyze the physical properties of the AGN components derived from our modeling (Section 5.2). Our main findings are as follows:

- A simple power-law ($L_\nu \propto \nu^\alpha$), is unable to replicate the radio emission from our sources when complex radio structures (i.e., lobes, jets, cores, hot spots) are present (Section 4.1).
- We predict that in half of our quasar sample there is a significant ($> 70\%$) non-thermal contribution at submm wavelengths. To robustly estimate the SFR, when including submm observations in the fit, it is important to subtract this source of contamination from the broadband photometry (Section 4.2).
- The median properties of the best fit torus parameters and their associated 25th-75th percentile ranges are: the inner radius of the torus, $R_{in} = 2.8^{+4.5}_{-1.8}$ (pc), the filling factor of the clumps, $V_C = 1.5^{+7.7}_{-1.5}$, the optical depth of the clumps, $\tau_C = 4.5^{+45}_{-0.0}$, the optical depth of the homogeneous disk, $\tau_D = 300^{+1000}_{-300}$ (Section 5.4).
- The median properties of the best-fit accretion disk parameters and their associated 25th-75th percentile ranges are as follows: The mass of the SMBHs $M_{BH}/M_\odot = 2.9^{+6.0}_{-1.8} (\times 10^9)$, the Eddington ratio $\log(\lambda_{Edd}) = -1.0^{+0.6}_{-1.2}$, the dimensionless spin parameter $a(\equiv Jc/GM_{BH}^2) = 0.98^{+0.99}_{-0.93}$. The SMBH properties estimated by ARXSED agree

with those in the literature for similarly defined samples (Section 5.4).

- The average inclination angles from the best fit torus and accretion disk are $48^\circ \pm 13^\circ$ and $50^\circ \pm 11^\circ$, respectively. The average inclination angle of the radio jets reported in the literature for our sample is $33^\circ \pm 14^\circ$. We do not find a statistically significant correlation between the jet inclination angle and the inclination angle from our best fit torus/accretion disk model. We speculate that this misalignment could occur after the jets are launched (Section 5.3).
- The quasars in our sample have a limited range of the radio core dominance, R_{CD} . To investigate the relation of the R_{CD} with the torus or accretion disk parameters, edge-on sources with wider range of R_{CD} should be considered as well. We defer any conclusion until we have fit the SEDs of the radio galaxies and their best fit torus/accretion disk parameters are available (Section 5.3).
- We present the median intrinsic SED of the radio-loud quasars at $1 < z \lesssim 2$. We find that the median SED of Elvis et al. (1994), obtained based on a sample of radio-loud quasars at $z < 1$ can not describe the SED of the radio-selected AGN at $z > 1$. The difference between the two median SED could be due to the sample selection, redshift and observations limitiaon (Section 5.5).
- Our SED models successfully reproduce the observed photometry and constrain the parameters describing the structures surrounding SMBHs at $z > 1$. Given the large number of parameters, diverse data quality, and possible variability which may bias our SED fits, we apply priors to the fits based on independent measurements of parameters such as M_{BH} from the literature. This helps to ensure consistency of the SED fitting results which otherwise may not be unique.

ACKNOWLEDGEMENTS

Support for this work was provided by the National Aeronautics and Space Administration and the *Chandra* X-ray Center (CXC), which is operated by the Smithsonian Astrophysical Observatory for and on behalf of the National Aeronautics Space Administration under contract NAS8-03060 (BJW, MAz,JK).

The scientific results in this article are based to a significant degree on observations made by the *Chandra* X-ray Observatory (CXO). This research has made use of data obtained from the *Chandra* Data Archive.

This research has made use of data provided by the National Radio Astronomy Observatory which is a facility of the National Science Foundation operated under cooperative agreement by Associated Universities, Inc. and data from the Sloan Digital Sky Survey (SDSS). Funding for the SDSS and SDSS-II has been provided by the Alfred P. Sloan Foundation, the Participating Institutions, the National Science Foundation, the U.S. Department of Energy, the National Aeronautics and Space Administration, the Japanese Monbukagakusho,

the Max Planck Society, and the Higher Education Funding Council for England. The SDSS Web Site is <http://www.sdss.org/>. The SDSS is managed by the Astrophysical Research Consortium for the Participating Institutions. The Participating Institutions are the American Museum of Natural History, Astrophysical Institute Potsdam, University of Basel, University of Cambridge, Case Western Reserve University, University of Chicago, Drexel University, Fermilab, the Institute for Advanced Study, the Japan Participation Group, Johns Hopkins University, the Joint Institute for Nuclear Astrophysics, the Kavli Institute for Particle Astrophysics and Cosmology, the Korean Scientist Group, the Chinese Academy of Sciences (LAMOST), Los Alamos National Laboratory, the Max-Planck-Institute for Astronomy (MPIA), the Max-Planck-Institute for Astrophysics (MPA), New Mexico State University, Ohio State University, University of Pittsburgh, University of Portsmouth, Princeton University, the United States Naval Observatory, and the University of Washington.

This research is based on observations made by *Herschel*, which is an ESA space observatory with science instruments provided by European-led Principal Investigator consortia and with important participation from NASA. This work is based in part on observations made with the Spitzer Space Telescope, which was operated by the Jet Propulsion Laboratory, California Institute of Technology under a contract with NASA.

We acknowledge the use of Ned Wright's calculator (Wright 2006) and NASA/IPAC Extragalactic Database (NED), operated by the Jet Propulsion Laboratory, California Institute of Technology, under contract with the National Aeronautics and Space Administration.

We acknowledge the use of IRAF which is distributed by the National Optical Astronomy Observatories, and operated by the Association of Universities for Research in Astronomy, Inc., under contract to the National Science Foundation.

REFERENCES

- Aird, J., et al. 2012, *ApJ*, 746, 90
 Akujor, C. E., & Garrington, S. T. 1995, *A&AS*, 112, 235
 Akujor, C. E., Spencer, R. E., & Saikia, D. J. 1991, *A&A*, 249, 337
 Akujor, C. E., et al. 1994, *A&AS*, 105, 247
 Aldcroft, T. L., et al. 2003, *ApJ*, 597, 751
 Anderson, S. F., et al. 1987, *AJ*, 94, 278
 Arshakian, T. G. 2005, *A&A*, 436, 817
 Aslanian, A. M., et al. 1968, *Astrofizika*, 4, 129
 Azadi, M., et al. 2015, *ApJ*, 806, 187
 Azadi, M., et al. 2017, *ApJ*, 835, 27
 Barthel, P., & Versteeg, J. 2019, *The Messenger*, 176, 37
 Barthel, P. D., Tytler, D. R., & Thomson, B. 1990, *A&AS*, 82, 339
 Baskin, A., & Laor, A. 2005, *MNRAS*, 356, 1029
 Becker, R. H., et al. 2000, *ApJ*, 538, 72
 Becker, R. H., et al. 2001, *ApJS*, 135, 227
 Benn, C. R., et al. 1998, *MNRAS*, 295, 451
 Bernhard, E., et al. 2016, *MNRAS*, 460, 902
 Berta, S., et al. 2013, *A&A*, 551, A100
 Best, P. N., & Heckman, T. M. 2012, *MNRAS*, 421, 1569
 Best, P. N., et al. 2005, *MNRAS*, 362, 25
 Best, P. N., et al. 2007, *MNRAS*, 379, 894
 Bianchi, S., et al. 2009, *A&A*, 495, 421
 Blandford, R. D., & Königl, A. 1979, *ApJ*, 232, 34
 Blandford, R. D., & Znajek, R. L. 1977, *MNRAS*, 179, 433
 Boquien, M., et al. 2019, *A&A*, 622, A103
 Braatz, J. A., et al. 1993, *ApJ*, 409, L5

- Braude, S. Y., et al. 1969, *MNRAS*, 143, 289
- Braude, S. Y., et al. 1970, *Astrophys. Lett.*, 5, 129
- Bremer, M. N., et al. 1992, *MNRAS*, 254, 614
- Bridle, A. H., et al. 1994, *AJ*, 108, 766
- Brotherton, M. S., et al. 2001, *ApJ*, 546, 775
- Brown, A., et al. 2019, *ApJ*, 871, 87
- Bruzual, G., & Charlot, S. 2003, *MNRAS*, 344, 1000
- Burns, J. O. 1990, *AJ*, 99, 14
- Cameron, M., et al. 1993, *ApJ*, 419, 136
- Capellupo, D. M., et al. 2016, *MNRAS*, 460, 212
- Chabrier, G. 2003, *PASP*, 115, 763
- Charlot, S., & Fall, S. 2000, *ApJ*, 539, 718
- Cleary, K., et al. 2007, *ApJ*, 660, 117
- Cohen, A. S., et al. 2004, *ApJS*, 150, 417
- Cohen, A. S., et al. 2007, *AJ*, 134, 1245
- Colla, G., et al. 1970, *A&AS*, 1, 281
- Colla, G., et al. 1972, *A&AS*, 7, 1
- Colla, G., et al. 1973, *A&AS*, 11, 291
- Collinson, J. S., et al. 2015, *MNRAS*, 449, 2174
- Collinson, J. S., et al. 2017, *MNRAS*, 465, 358
- Condon, J. J., et al. 1983, *AJ*, 88, 20
- Condon, J. J., et al. 1998, *AJ*, 115, 1693
- Conway, J. E. 2002, *??inNew A Rev.*, 46, 263
- Coziol, R., et al. 2017, *MNRAS*, 466, 921
- Crummy, J., et al. 2006, *MNRAS*, 365, 1067
- Cutri, R. M., et al. 2001, in *American Astronomical Society Meeting Abstracts*, Vol. 198, American Astronomical Society Meeting Abstracts #198, 33.17
- Czerny, B., et al. 2003, *A&A*, 412, 317
- da Cunha, E., Charlot, S., & Elbaz, D. 2008, *MNRAS*, 388, 1595
- da Cunha, E., et al. 2015, *ApJ*, 806, 110
- Daly, R. A. 2011, *MNRAS*, 414, 1253
- Daly, R. A. 2019, *ApJ*, 886, 37
- Davis, S. W., & Laor, A. 2011, *ApJ*, 728, 98
- Done, C., et al. 2012, *MNRAS*, 420, 1848
- Douglas, J. N., et al. 1996, *AJ*, 111, 1945
- Drouart, G., et al. 2014, *A&A*, 566, A53
- Edelson, R. A., & Malkan, M. A. 1986, *ApJ*, 308, 59
- Efstathiou, A., & Rowan-Robinson, M. 1995, *MNRAS*, 273, 649
- Elvis, M. 2010, in *IAU Symposium*, Vol. 267, Co-Evolution of Central Black Holes and Galaxies, ed. B. M. Peterson, R. S. Somerville, & T. Storchi-Bergmann, 55–64. [link]
- Elvis, M., et al. 1994, *ApJS*, 95, 1
- Elvis, M., et al. 2012, *ApJ*, 759, 6
- Fabian, A. C., Celotti, A., & Johnstone, R. M. 2003, *MNRAS*, 338, L7
- Fanaroff, B. L., & Riley, J. M. 1974, *MNRAS*, 167, 31P
- Fanti, C., et al. 1974, *A&AS*, 18, 147
- Fanti, C., et al. 1989, *A&A*, 217, 44
- Feltre, A., et al. 2012, *MNRAS*, 426, 120
- Fernini, I., Burns, J. O., & Perley, R. A. 1997, *AJ*, 114, 2292
- Ficarra, A., Grueff, G., & Tomassetti, G. 1985, *A&AS*, 59, 255
- Fioc, M., & Rocca-Volmerange, B. 2019, *A&A*, 623, A143
- Foley, A. R., & Barthel, P. D. 1990, *A&A*, 228, 17
- Fritz, J., Franceschini, A., & Hatziminaoglou, E. 2006, *MNRAS*, 366, 767
- Geach, J. E., et al. 2011, *ApJ*, 730, L19
- Geldzahler, B. J., & Witzel, A. 1981, *AJ*, 86, 1306
- Georgakakis, A., et al. 2009, *MNRAS*, 394, 533
- Ghisellini, G. 2013, *Radiative Processes in High Energy Astrophysics*, Vol. 873. [link]
- Gierliński, M., & Done, C. 2004, *MNRAS*, 349, L7
- Gower, J. F. R., Scott, P. F., & Wills, D. 1967, *MNRAS*, 71, 49
- Gregory, P. C., & Condon, J. J. 1991, *ApJS*, 75, 1011
- Grewing, M., Demoulin, M.-H., & Burbidge, G. R. 1968, *ApJ*, 154, 447
- Grimes, J. A., Rawlings, S., & Willott, C. J. 2005, *MNRAS*, 359, 1345
- Haardt, F., & Maraschi, L. 1993, *ApJ*, 413, 507
- Hales, S. E. G., Baldwin, J. E., & Warner, P. J. 1993, *MNRAS*, 263, 25
- Hales, S. E. G., et al. 1990, *MNRAS*, 246, 256
- Hales, S. E. G., et al. 1995, *MNRAS*, 274, 447
- Hamann, F. W., et al. 2001, *ApJ*, 550, 142
- Hao, H., et al. 2014, *MNRAS*, 438, 1288
- Hardcastle, M. J., & Croston, J. H. 2020, *arXiv e-prints*, arXiv:2003.06137
- Heckman, T. M., & Best, P. N. 2014, *ARA&A*, 52, 589
- Heckman, T. M., et al. 2004, *ApJ*, 613, 109
- Hilbert, B., et al. 2016, *ApJS*, 225, 12
- Hönig, S. F., & Kishimoto, M. 2010, *A&A*, 523, A27
- Hönig, S. F., et al. 2013, *ApJ*, 771, 87
- Hunt, A. M. L. K. 2003, *ApJL*, 589, L21
- Ishwara-Chandra, C. H., Dwarakanath, K. S., & Anantharamaiah, K. R. 2003, *Journal of Astrophysics and Astronomy*, 24, 37
- Janssen, R. M. J., et al. 2012, *A&A*, 541, A62
- Jester, S. 2005, *ApJ*, 625, 667
- Kellermann, K. I., & Pauliny-Toth, I. I. K. 1973, *AJ*, 78, 828
- Kellermann, K. I., Pauliny-Toth, I. I. K., & Williams, P. J. S. 1969, *ApJ*, 157, 1
- Kellermann, K. I., et al. 1989, *AJ*, 98, 1195
- Kellermann, K. I., et al. 2016, *ApJ*, 831, 168
- Kim, D., & Im, M. 2018, *A&A*, 610, A31
- King, A. 2016, *MNRAS*, 456, L109
- Kirkpatrick, A., et al. 2017, *ApJ*, 849, 111
- Kishimoto, M., et al. 2011, *A&A*, 527, A121
- Konigl, A. 1981, *ApJ*, 243, 700
- Kriek, M., et al. 2009, *ApJ*, 700, 221
- Krügel, E. 2009, *A&A*, 493, 385
- Krügel, E., & Siebenmorgen, R. 1994, *A&A*, 288, 929
- Kubota, A., & Done, C. 2018, *MNRAS*, 480, 1247
- Kuehr, H., et al. 1981, *A&AS*, 45, 367
- Kuraszkiewicz, J. K., et al. 2002, *ApJS*, 143, 257
- Kuraszkiewicz, J. K., et al. 2003, *ApJ*, 590, 128
- Lacy, M., et al. 2004, *ApJS*, 154, 166
- Laing, R. A., & Peacock, J. A. 1980, *MNRAS*, 190, 903
- Laing, R. A., Riley, J. M., & Longair, M. S. 1983, *MNRAS*, 204, 151
- Lani, C., Netzer, H., & Lutz, D. 2017, *MNRAS*, 471, 59
- Laor, A. 2000, *ApJ*, 543, L111
- Laor, A., & Davis, S. W. 2014, *MNRAS*, 438, 3024
- Large, M. I., et al. 1981, *MNRAS*, 194, 693
- Lee, S.-K., et al. 2010, *ApJ*, 725, 1644
- Leipski, C., et al. 2010, *ApJ*, 717, 766
- Leja, J., et al. 2017, *ApJ*, 837, 170
- Leja, J., et al. 2018, *ApJ*, 854, 62
- Liu, R., Pooley, G., & Riley, J. M. 1992, *MNRAS*, 257, 545
- Liu, Y., Jiang, D. R., & Gu, M. F. 2006, *ApJ*, 637, 669
- Lonsdale, C. J., & Barthel, P. D. 1984, *A&A*, 135, 45
- Lonsdale, C. J., & Barthel, P. D. 1986, *AJ*, 92, 12
- Lonsdale, C. J., Barthel, P. D., & Miley, G. K. 1993, *ApJS*, 87, 63
- Ludke, E., et al. 1998, *MNRAS*, 299, 467
- Mack, K. H., et al. 2005, *A&A*, 435, 863
- Madau, P., & Dickinson, M. 2014, *ARA&A*, 52, 415
- Mantovani, F., et al. 1992, *MNRAS*, 257, 353
- Marin, F., & Antonucci, R. 2016, *ApJ*, 830, 82
- Markwardt, C. B. 2009, in *Astronomical Society of the Pacific Conference Series*, Vol. 411, Astronomical Data Analysis Software and Systems XVIII, ed. D. A. Bohlender, D. Durand, & P. Dowler, 251. [link]
- McLure, R. J., & Dunlop, J. S. 2002, *MNRAS*, 331, 795
- McLure, R. J., et al. 2006, *MNRAS*, 368, 1395
- Middei, R., et al. 2018, *arXiv e-prints*, arXiv:1803.07334
- Mullaney, J. R., et al. 2011, *MNRAS*, 414, 1082
- Nenkova, M., et al. 2008, *ApJ*, 685, 147
- Netzer, H., et al. 2007, *ApJ*, 666, 806
- Neugebauer, G., et al. 1979, *ApJ*, 230, 79
- Novikov, I. D., & Thorne, K. S. 1973, in *Black Holes (Les Astres Occlus)*, 343–450
- O’Dea, C. P. 1998, *PASP*, 110, 493
- Orr, M. J. L., & Browne, I. W. A. 1982, *MNRAS*, 200, 1067
- Page, M. J., et al. 2012, *Nature*, 485, 213
- Pauliny-Toth, I. I. K., Wade, C. M., & Heeschen, D. S. 1966, *ApJS*, 13, 65
- Petrucchi, P. O., et al. 2001, *ApJ*, 556, 716
- Petrucchi, P. O., et al. 2013, *A&A*, 549, A73
- Petrucchi, P. O., et al. 2018, *A&A*, 611, A59
- Piconcelli, E., et al. 2005, *A&A*, 432, 15
- Pier, E. A., & Krolik, J. H. 1992, *ApJ*, 401, 99
- Podigachoski, P., et al. 2015, *A&A*, 575, A80
- Podigachoski, P., et al. 2016a, *MNRAS*, 462, 4183
- Podigachoski, P., et al. 2016b, *A&A*, 585, A142
- Polletta, M., et al. 2000, *A&A*, 362, 75
- Polletta, M., et al. 2007, *ApJ*, 663, 81

- Rees, M. J. 1984, *ARA&A*, 22, 471
- Reynolds, C. S. 2019, *Nature Astronomy*, 3, 41
- Richards, G. T., et al. 2006, *ApJS*, 166, 470
- Rieke, G. H., & Lebofsky, M. J. 1981, *ApJ*, 250, 87
- Roche, P. F., et al. 1991, *MNRAS*, 248, 606
- Rosario, D. J., et al. 2012, *A&A*, 545, A45
- Rovilos, E., et al. 2012, *A&A*, 546, A58
- Rowan-Robinson, M. 1995, *MNRAS*, 272, 737
- Salvesen, G., et al. 2009, *ApJ*, 692, 753
- Sandage, A. R. 1971, in *Study Week on Nuclei of Galaxies*, ed. D. J. K. O’Connell, 271
- Sanitt, N. 1976, *MNRAS*, 174, 91
- Shakura, N. I., & Sunyaev, R. A. 1976, *MNRAS*, 175, 613
- Shang, Z., et al. 2011, *ApJS*, 196, 2
- Shangguan, J., et al. 2020, *ApJ*, 899, 112
- Shen, Y. 2013, *Bulletin of the Astronomical Society of India*, 41, 61
- Shimmins, A. J., & Wall, J. V. 1973, *Australian Journal of Physics*, 26, 93
- Siebenmorgen, R., Heymann, F., & Efstathiou, A. 2015, *A&A*, 583, A120
- Siebenmorgen, R., Voshchinnikov, N. V., & Bagnulo, S. 2014, *A&A*, 561, A82
- Siebenmorgen, R., et al. 2005, *Astronomische Nachrichten*, 326, 556
- Siemiginowska, A., et al. 2010, *ApJ*, 722, 102
- Slee, O. B. 1995, *Australian Journal of Physics*, 48, 143
- Smith, H. E., & Spinrad, H. 1980, *PASP*, 92, 553
- Spencer, R. E., et al. 1991, *MNRAS*, 250, 225
- Spinrad, H., et al. 1985, *PASP*, 97, 932
- Steppe, H., et al. 1995, *A&AS*, 113, 409
- Suganuma, M., et al. 2006, *ApJ*, 639, 46
- Sulentic, J. W., et al. 2002, *ApJ*, 566, L71
- Svensson, R., & Zdziarski, A. A. 1994, *ApJ*, 436, 599
- Tody, D. 1986, in *Society of Photo-Optical Instrumentation Engineers (SPIE) Conference Series*, Vol. 627, *Instrumentation in astronomy VI*, ed. D. L. Crawford, 733. [\[link\]](#)
- Urry, C. M., & Padovani, P. 1995, *PASP*, 107, 803
- Vanden Berk, D. E., et al. 2006, *AJ*, 131, 84
- Viner, M. R., & Erickson, W. C. 1975, *AJ*, 80, 931
- Waldram, E. M., et al. 1996, *MNRAS*, 282, 779
- Westhues, C., et al. 2016, *AJ*, 151, 120
- Wilkes, B. 2011, *The Environmental Impact of the High-redshift (1.532) Radio-Loud Quasars 3C270.1*, *Chandra Proposal*
- Wilkes, B. J., et al. 2013, *ApJ*, 773, 15
- Willott, C. J., Martínez-Sansigre, A., & Rawlings, S. 2007, *AJ*, 133, 564
- Willott, C. J., et al. 2000, *MNRAS*, 316, 449
- Willott, C. J., et al. 2002, *MNRAS*, 331, 435
- Wills, B. J. 1975, *Australian Journal of Physics Astrophysical Supplement*, 38, 1
- Wright, A., & Otrupcek, R. 1990, *PKS Catalog (1990)*, 0
- Wright, E. L. 2006, *PASP*, 118, 1711
- Zhang, S. N., Cui, W., & Chen, W. 1997, *ApJ*, 482, L155

APPENDIX

Table A1, A2 and A3 below presents high, medium and low frequency radio data used in the SED analysis in this study with their references. The fluxes densities are in Jansky.

Table 1
High frequency radio data

Name	230 GHz	90 GHz	31.4 GHz	14900 MHz	10700 MHz	8870 MHz	8400 MHz	8085 MHz	5000 MHz	4.85 GHz	2695 MHz
3C 9				0.130 ± 0.010 L80	0.216 ± 0.019 L80				0.546 ± 0.050 L80	0.482 ± 0.066 G91	0.981 ± 0.040 L80
3C 14				0.150 ± 0.010 L80	0.216 ± 0.019 L80				0.606 ± 0.030 L80	0.549 ± 0.075 G91	1.021 ± 0.040 L80
3C 43	0.064 ± 0.010 SJ95	0.189 ± 0.042 SJ95		0.450 ± 0.010 L80	0.610 ± 0.038 L80				1.082 ± 0.040 L80	1.173 ± 0.157 G91	1.698 ± 0.040 L80
3C 181				0.200 ± 0.010 L80	0.291 ± 0.019 L80				0.655 ± 0.050 L80	0.675 ± 0.092 G91	1.254 ± 0.040 L80
3C 186					0.084 ± 0.014 L80				0.377 ± 0.050 L80	0.308 ± 0.038 G91	0.586 ± 0.040 L80
3C 190				0.300 ± 0.010 L80	0.356 ± 0.019 L80				0.814 ± 0.060 L80	0.694 ± 0.095 G91	1.395 ± 0.051 L80
3C 191				0.180 ± 0.010 L80	0.225 ± 0.019 L80				0.457 ± 0.060 L80	0.559 ± 0.077 G91	0.960 ± 0.040 L80
3C 204				0.110 ± 0.010 L80	0.159 ± 0.015 L80				0.338 ± 0.030 L80	0.369 ± 0.033 G91	0.505 ± 0.040 L80
3C 205				0.160 ± 0.010 L80	0.234 ± 0.019 L80				0.665 ± 0.040 L80	0.688 ± 0.070 G91	1.122 ± 0.040 L80
3C 208				0.140 ± 0.010 L80	0.234 ± 0.019 L80				0.536 ± 0.050 L80	0.506 ± 0.069 G91	0.960 ± 0.040 L80
3C 212				0.480 ± 0.010 L80	0.497 ± 0.019 L80				0.884 ± 0.040 L80	0.746 ± 0.102 G91	1.426 ± 0.040 L80
3C 245			0.94 ± 0.15 G81	0.850 ± 0.010 L80	0.966 ± 0.038 L80	1.04 ± 0.04 S73			1.380 ± 0.040 L80	1.742 ± 0.240 G91	2.19 ± 0.01 W75
3C 268.4				0.180 ± 0.010 L80	0.244 ± 0.019 L80				0.596 ± 0.030 L80	0.608 ± 0.072 G91	1.072 ± 0.040 L80
3C 270.1				0.440 ± 0.010 L80	0.450 ± 0.019 L80				0.864 ± 0.040 L80	0.875 ± 0.111 G91	1.506 ± 0.040 L80
3C 287	0.116 ± 0.020 SJ95	0.512 ± 0.090 SJ95		1.420 ± 0.030 L80	1.726 ± 0.047 L80			2.20 ± 0.18 C83	3.237 ± 0.060 L80	3.106 ± 0.413 G91	4.651 ± 0.061 L80
3C 318				0.230 ± 0.010 L80	0.319 ± 0.019 L80				0.745 ± 0.030 L80	0.852 ± 0.115 G91	1.345 ± 0.040 L80
3C 325				0.250 ± 0.020 L80	0.394 ± 0.019 L80				0.824 ± 0.040 L80	1.050 ± 0.099 G91	1.860 ± 0.040 L80
4C 16.49									0.320 ± 0 W90	0.345 ± 0.047 G91	0.680 ± 0 W90
3C 432				0.080 ± 0.010 L80	0.131 ± 0.015 L80				0.308 ± 0.060 L80	0.407 ± 0.055 G91	0.768 ± 0.040 L80
3C 454.0				0.300 ± 0.010 L80	0.394 ± 0.028 L80				0.784 ± 0.030 L80	0.787 ± 0.107 G91	1.223 ± 0.040 L80

Table 2
Medium frequency radio data

Name	1400 MHz	750 MHz	635 MHz	408 MHz	365 MHz	326MHz	178 MHz	160 MHz	151 MHz	86 MHz
3C 9	1.955 ± 0.123 L80	3.890 ± 0.189 L80		7.79 ± 0.32 L81						35.700 ± 1.600 L80
3C 14	1.873 ± 0.103 L80	3.580 ± 0.206 L80		5.85 ± 0.18 L81	6.830 ± 0.086 D96		11.336 ± 1.134 L80			24.400 ± 2.700 L80
3C 43	2.819 ± 0.082 L80	4.280 ± 0.182 L80		6.440 ± 0.515 F74	8.556 ± 0.084 D96		12.644 ± 1.264 L80	16.3 ± 2.40 K81		20.500 ± 4.400 L80
3C 181	2.3044 ± 0.691 C98	3.760 ± 0.171 L80		6.73 ± 0.21 L81	7.624 ± 0.156 D96		15.805 ± 0.790 L80			24.200 ± 2.200 L80
3C 186	1.2369 ± 0.0371 C98	2.740 ± 0.167 L80		5.55 ± 0.11 F85	6.582 ± 0.109 D96		15.369 ± 0.768 L80		15.59 ± 0.075 H93	33.200 ± 2.700 L80
3C 190	2.552 ± 0.072 L80	4.300 ± 0.174 L80		7.63 ± 0.24 L81	9.088 ± 0.090 D96		16.350 ± 0.818 L80			26.800 ± 2.700 L80
3C 191	1.8498 ± 0.0555 C98	3.440 ± 0.170 L80		7.32 ± 0.32 L81	7.485 ± 0.083 D96		14.170 ± 0.709 L80			34.300 ± 1.600 L80
3C 204	1.297 ± 0.082 L80	2.370 ± 0.060 P66		7.32 ± 0.32 L81	5.491 ± 0.166 D96	7.485	11.445 ± 0.572 L80			29.6 ± 1.100 L80
3C 205	2.387 ± 0.072 L80	3.950 ± 0.176 L80			9.276 ± 0.200 D96		13.734 ± 1.373 L80			39.200 ± 4.400 L80
3C 208	2.3648 ± 0.0709 C98	4.560 ± 0.175 L80		7.75 ± 0.25 L81	10.332 ± 0.178 D96		20.165 ± 1.008 L80			41.500 ± 2.400 L80
3C 212	2.3713 ± 0.0711 C98	4.440 ± 0.183 L80		7.01 ± 0.22 L81	8.337 ± 0.151 D96		16.459 ± 0.823 L80			29.800 ± 3.100 L80
3C 245	3.3062 ± 0.0992 C98	5.060 ± 0.178 L80		8.90 ± 0.37 L81	9.449 ± 0.210 D96		15.696 ± 0.785 L80			27.400 ± 1.100 L80
3C 268.4	1.9804 ± 0.0594 C98	3.620 ± 0.174 L80		5.69 ± 0.12 F85	6.585 ± 0.119 D96		11.227 ± 0.561 L80			22.400 ± 2.700 L80
3C 270.1	2.727 ± 0.072 L80	5.04 ± 0.09 P66		8.200 ± 0.41 C70	9.742 ± 0.134 D96		14.824 ± 0.741 L80			30.800 ± 2.700 L80
3C 287	7.0526 ± 0.2116 C90	9.670 ± 0.251 L80		11.942 ± 0.955 C72	14.959 ± 0.282 D96		17.440 ± 0.872 L80	20.3 ± 3.00 K81	15.53 ± 0.699 W96	19.400 ± 2.200 L80
3C 318	2.562 ± 0.072 L80	2.6885 ± 0.0807 C98	4.440 ± 0.183 L80			9.212 ± 0.085 D96		13.407 ± 0.670 L80		13.98 ± 0.643 W96
3C 325	3.5645 ± 0.1253 C98	6.190 ± 0.194 L80			12.124 ± 0.295 D96		17.004 ± 0.850 L80			33.100 ± 2.700 L80
4C 16.49	1.4565 ± 0.0511 C98			5.36 ± 0.17 L81	6.268 ± 0.098 D96		10.5 ± 0.84 G67			
3C 432	1.5792 ± 0.0557 C98	2.900 ± 0.167 L80		6.05 ± 0.15 L81	6.484 ± 0.116 D96		11.990 ± 1.199 L80			21.100 ± 1.900 L80
3C 454.0	2.140 ± 0.072 L80	3.460 ± 0.170 L80		5.65 ± 0.18 L81	6.485 ± 0.054 D96		12.644 ± 0.632 L80			

Table 3
Low frequency radio data

Name	80MHz	74 MHz	60 MHz	38 MHz	26.3 MHz	25.0MHz	22.25 MHz	20.0 MHz	16.7 MHz	14.7 MHz	12.6 MHz	10 MHz
3C 9			53.015 ± 7.048 A68	75.520 ± 7.552 L80	99.000 ± 18.000 L80		97.750 ± 16.667 L80					204.000 ± 42.000 L80
3C 14				42.480 ± 8.496 L80	69.000 ± 7.000 L80							
3C 43	23.004 ± 3.019 K81			46.020 ± 9.204 L80	46.000 ± 6.000 L80		69.000 ± 8.333 L80					
3C 181			54.013 ± 4.011 A68	37.760 ± 7.552 L80	57.000 ± 8.000 L80							
3C 186			42.015 ± 3.008 A68	57.820 ± 5.782 L80	54.000 ± 7.000 L80	77.000 ± 24.000 B70	54.050 ± 5.000 L80	61.000 ± 17.000 B70	103 ± 35 B70	126 ± 45 B70	120 ± 47 B70	
3C 190			40.120 ± 8.024	64. ± 8. L80	V75	71.300 ± 11.667						192.000 ± 42.000 L80
3C 191				56.640 ± 5.664 L80	46.000 ± 8.000 L80		96.600 ± 11.667 L80	120.000 ± 18.000 B69	160. ± 32 B69	300. ± 66 B69	380. ± 84 B69	276.000 ± 66.000 L80
3C 204		26.64 ± 2.71 C07	34.0 ± 3.00 A68	58.9 ± 10.0 H95		101 ± 19.2 B70		95.00 ± 19.00 B70	131± 26.2 B70		380. ± 84 B70	
3C 205				54.280 ± 5.428 L80	60.000 ± 10.000 L80			88.000± 16.7 B70	85 ± 16.2 B70	130 ± 28.6 B70	147 ± 32.3 B70	162.0 ± 36.0 L80
3C 208			42.016± 3.008 A68	68.440 ± 6.844 L80	83.000 ± 10.000 L80		67.850 ± 21.667 L80					
3C 212			46.015± 4.014 A68				29.900 ± 11.667 L80					
3C 245			34.010 ± 5.041 A68	47.200 ± 4.720 L80	73.000 ± 8.000 L80		64.400 ± 11.667 L80	137.000 ± 57.5 B70	125 ± 35 B70	132 ± 27.7 B70	161 ± 45.1 B70	170.400 ± 39.600 L80
3C 268.4		20.72 ± 3.79 M05		36.580 ± 7.316 L80	34.000 ± 8.000 L80							
3C 270.1		30.8 ± 0 C04		33.040 ± 6.608 L80	60.000 ± 8.000 L80		60.950 ± 10.000 L80	85.000 ± 30.000 B70	141 ± 65 B70	210 ± 61 B70		
3C 287				30.680 ± 6.136 L80		65.000 ± 21.000 B69		120. ± 50.4 B69	140. ± 61.6 B69	240. ± 120 B69	320. ± 160 B69	
3C 318					25.960 ± 7.788 L80	31.000 ± 7.000 L80		37.950 ± 3.334 L80				
3C 325				42.480 ± 4.248 L80								
4C 16.49					42. ± 9. V75							
3C 432				55.460 ± 11.092 L80	42.000 ± 7.000 L80		65.550 ± 8.333 L80					
3C 454.0			24.010 ± 3.019 A68	31.860 ± 9.558 L80								

References: A68 - Aslanian et al. (1968), B69 - Braude et al. (1969), B70 - Braude et al. (1970), C70 - Colla et al. (1970), C72 - Colla et al. (1972), C73 - Colla et al. (1973), C83 - Condon et al. (1983), C98 - Condon et al. (1998), C04 - Cohen et al. (2004), D96 - Douglas et al. (1996), F74 - Fanti et al. (1974), F85 - Ficarra et al. (1985), G67 - Gower et al. (1967), G81 - Geldzahler & Witzel (1981), G91 - Gregory & Condon (1991), H90 - Hales et al. (1990), H93 - Hales et al. (1993), H95 - Hales et al. (1995), K69 - Kellermann et al. (1969), K73 - Kellermann & Pauliny-Toth (1973), K81 - Kuehr et al. (1981), L80 - Laing & Peacock (1980), L81 - Large et al. (1981), M05 - Mack et al. (2005), P66 - Pauliny-Toth et al. (1966), S73 - Shimmins & Wall (1973), SJ95 - Steppe et al. (1995), S95 - Slee (1995), V75 - Viner & Erickson (1975), W75 - Wills (1975), W90 - Wright & Otrupcek (1990), W96 - WalDRAM et al. (1996), C07- Cohen et al. (2007)